Thesis for The Degree of Licentiate of Engineering

Nonlinear Microwave Measurement Architectures for Wideband Device Characterization

Sebastian Gustafsson

CHALMERS

Microwave Electronics Laboratory
Department of Microtechnology and Nanoscience – MC2
Chalmers University of Technology
Gothenburg, Sweden, 2015

Nonlinear Microwave Measurement Architectures for Wideband Device Characterization

Sebastian Gustafsson

Chalmers University of Technology
Department of Microtechnology and Nanoscience – MC2
Microwave Electronics Laboratory
SE-412 96 Gothenburg, Sweden
Phone: +46 (0) 31 772 1000

Technical report MC2-313
ISSN 1652-0769

Printed by Chalmers Reproservice
Gothenburg, Sweden 2015

Abstract

The global surge for ubiquitous mobile communication requiring high speed and high capacity cellular networks has resulted in a golden age for the development of wireless technology. Modern cellular standards employ complex modulation formats with wider signal bandwidths to cope with the growing demand. The increasing complexity of wireless systems, however, directly translates into a need for more detailed characterization using advanced measurement setups. Furthermore, new semiconductor material technologies such as gallium nitride (GaN) are utilized to enable higher performance in microwave circuits. As GaN-based devices tend to suffer from slow and fast dispersion phenomena, relevant wideband characterization is needed.

The main focus of this thesis is on the implementation of a wideband two-port nonlinear measurement setup, consisting of a real-time oscilloscope (RTO) with 4 GHz bandwidth as a measurement receiver. The large instantaneous bandwidth enables new types of measurement scenarios to be carried out. The measurement setup was demonstrated by its use as an active load-pull setup, where the efficiency of a GaN high electron mobility transistor (HEMT) was improved by tuning the load impedances at intermodulation frequencies. Moreover, due to nonidealities in the microwave front-end of the oscilloscope, a correction technique was developed to improve signal fidelity of the acquired waveforms in the system over a large dynamic range.

Furthermore, device characterization was carried out on in-house processed GaN HEMTs, and investigations on how dispersive effects manifest on various DC and RF performance aspects were made. As concluded from the measurements, dispersive phenomena are extremely dynamic and cause complex device behavior. These results express the need for wideband characterization, enabled by the proposed measurement setup, to further understand dispersion and its influence on system performance.

The results in this thesis enables future research activities within wideband device characterization, which is essential for the design of high performance microwave circuits for next generation wireless systems.

Keywords: Nonlinear characterization, microwave, wideband, oscilloscope, active load-pull, GaN HEMT

List of Publications

Appended Publications

This thesis is based on the following papers:

[A] **S. Gustafsson**, M. Thorsell and C. Fager, "A Novel Active Load-pull System with Multi-band Capabilities," *2013 81st ARFTG Microwave Measurement Conference*, pp. 1–4, June, 2013.

[B] **S. Gustafsson**, M. Thorsell, J. Stenarson and C. Fager, "An Oscilloscope Correction Method for Vector-Corrected RF Measurements," Accepted for publication in *IEEE Transactions on Instrumentation and Measurement*, 2015.

[C] **S. Gustafsson**, J.-T. Chen, J. Bergsten, U. Forsberg, M. Thorsell, E. Janzen and N. Rorsman, "Dispersive Effects in Microwave AlGaN /AlN/GaN HEMTs With Carbon-Doped Buffer," *IEEE Transactions on Electron Devices*, vol. 62, iss. 7, pp. 2162–2169, May, 2015.

Other Publications

The following papers have been accepted for publication but are not included in the thesis. The content partially overlaps with the appended papers or is out of the scope of this thesis.

[a] J. Bergsten, J.-T. Chen, **S. Gustafsson**, A. Malmros, U. Forsberg, M. Thorsell, E. Janzen and N. Rorsman, "Performance Enhancement of Microwave GaN HEMTs Without an AlN-exclusion Layer Using an Optimized AlGaN/GaN Interface Growth Process," *Submitted to IEEE Transactions on Electron Devices*

[b] O. Axelsson, **S. Gustafsson**, H. Hjelmgren, N. Rorsman and M. Thorsell, "Application Relevant Evaluation of Memory Effects in AlGaN/GaN HEMTs with Fe doped buffer," *Submitted to IEEE Transactions on Electron Devices*

[c] T. Huang, A. Malmros, J. Bergsten, **S. Gustafsson**, O. Axelsson, M. Thorsell and N. Rorsman, "Suppression of Dispersive Effects in AlGaN/GaN High-Electron-Mobility Transistors Using Bilayer SiNx Grown by Low Pressure Chemical Vapor Deposition," *IEEE Electron Device Letters*, vol. 36, iss. 6, pp. 537–539, April, 2015.

[d] P. Landin, **S. Gustafsson**, C. Fager, and T. Eriksson, "WebLab: A Web-Based Setup for PA Digital Predistortion and Characterization," *IEEE Microwave Magazine*, vol. 16, iss. 1, pp. 138-140, February, 2015.

Notations and abbreviations

Notations

A_k	Amplitude coefficients
a_i	Traveling voltage wave at port i
b_i	Traveling voltage wave at port i
B	Bandwidth
C	Channel Capacity
C_{ds}	Drain-source capacitance
C_k	Fourier coefficients
C_T	Capacitance of output admittance dispersion model
c_{thru}	Through error coefficient
D_1	Activation energy of surface-related trap
E_2	Activation energy of buffer-related trap
e_{ij}	Error coefficients
f_0	Fundamental frequency
f_{IF}	Intermediate frequency
f_{max}	Maximum oscillation frequency
f_{RF}	Radio frequency
f_s	Sampling frequency
f_t	Current gain cutoff frequency
g_{ds}	Output conductance
g_m	Transconductance
I_{DS}	Drain-to-source current
k	Harmonic index
k_i	Complex correction factor for channel i
m	Modulation frequency index
m_i	Measured voltage at port i
N	Harmonic index
p_i	Harmonic coefficients
P_{DC}	DC power
P_{in}	Input power at radio frequency
P_{out}	Output power at radio frequency
r_{ij}	Auxiliary port error coefficients
r_T	Resistance of output admittance dispersion model

S_{ij}	S-parameters
$\boldsymbol{T_{DUT}}$	T-parameter matrix of DUT
$\boldsymbol{T_i}$	T-parameter matrix of error model
$\boldsymbol{T_m}$	Measured T-parameter matrix
t_s	Period time
V_{DS}	Drain-to-source voltage
V_{GS}	Gate-to-source voltage
$x(t)$	Input signal, time domain
$X(f)$	Input signal, frequency domain
$y(t)$	Output signal, time domain
$Y(f)$	Output signal, frequency domain
Y_{ij}	Y-parameters
Z_0	Characteristic impedance
α	Absolute magnitude and phase error coefficient
α_r	Abs. magn. and phase err. coeff. referenced to aux. plane
Γ_L	Load reflection coefficient
Γ_m	Measured load reflection coefficient
ω_0	Fundamental angular frequency
ω_c	Characteristic angular frequency
ω_{RF}	Angular frequency of radio frequency signal
ω_{LO}	Local oscillator angular frequency
τ	Pulse width

Abbreviations

2DEG	Two-dimensional Electron Gas
ADC	Analog-to-Digital Converter
AMPS	Advanced Mobile Phone System
AWG	Arbitrary Waveform Generator
BW	Bandwidth
CAD	Computer-Aided Design
CC	Current Collapse
CDMA	Code Division Multiple Access
CW	Continuous Wave
DAC	Digital-to-Analog Converter
DC	Direct Current
DC-HSDPA	Dual Cell High Speed Downlink Packet Access
DUT	Device Under Test
ENOB	Effective Number Of Bits
FET	Field Effect Transistor
FFT	Fast Fourier Transform
GaN	Gallium Nitride
GSM	Global System for Mobile Communications
HEMT	High Electron Mobility Transistor
HR	Highly Resistive
HSDPA	High Speed Downlink Packet Access

HSPA	High Speed Packet Access
IM3	Third Order Intermodulation
I-V	Current-Voltage
LO	Local Oscillator
LRM	Line-Reflect-Match
LSNA	Large Signal Network Analyzer
LTE	Long Term Evolution
MTA	Microwave Transition Analyzer
NVNA	Nonlinear Vector Network Analyzer
PAPR	Peak to Average Power Ratio
PISPO	Periodic In Same Periodic Out
QAM	Quadrature Amplitude Modulation
RF	Radio Frequency
RTO	Real Time Oscilloscope
SiC	Silicon Carbide
SNDR	Signal-to-Noise-and-Distortion Ratio
SNR	Signal-to-Noise Ratio
SOL	Short-Open-Load
SOLR	Short-Open-Load-Reciprocal
SOLT	Short-Open-Load-Through
TRL	Through-Reflect-Line
VGA	Variable Gain Amplifier
VNA	Vector Network Analyzer
WCDMA	Wideband Code Division Multiple Access
WLAN	Wireless Local Area Network

Contents

Chapter 1

Introduction

The future is truly wireless, and the drive towards ubiquitous mobile communication is inevitable. In 2014, we witnessed a unique event in the history of mobile communications; the number of mobile connected devices surpassed the world's population [1–4]. This staggering number will continue to grow, directly translating into deployment of higher capacity cellular networks. Furthermore, the consumer adoption of portable devices such as smartphones has fueled the exponential growth of mobile data traffic consumption. As cellular standards have evolved and enabled higher data rates for each new generation, so has the underlying technology, consisting of complex microwave circuits and advanced digital signal processing.

The theoretical upper bound in data throughput of a communications channel is set by the Shannon-Hartley theorem, which states that the maximum capacity (C) in terms of bitrate (bit/s) is linearly dependent on the channel bandwidth (B) and logarithmically dependent on the signal to noise ratio (SNR) in the channel, as [5]

$$C = B \log_2(1 + \mathrm{SNR}). \tag{1.1}$$

As a consequence of this, the need for higher data throughput has resulted in wider channel bandwidths and more spectral efficient modulation schemes. The former is illustrated in Fig. 1.1, which shows the increase in signal bandwidth for different wireless standards over recent years. The most recent wireless standards employ carrier aggregation techniques to combine available spectrum at different frequency bands [6]. An indirect result of the ongoing bandwidth expansion is that the frequency spectrum has become immensely crowded, which is planned to be mitigated by operation at higher carrier frequencies ($>$ 30 GHz) [7]. This, however, further complicates the design and characterization of microwave circuits. Operation at higher frequencies also requires exotic semiconductor materials such as gallium nitride (GaN) to maintain power performance.

Moreover, the use of spectral efficient modulation schemes has resulted in more dynamic signals with large amplitude modulation of the carrier signal. Consequently, the average signal power is low compared to the peak signal power. This can be problematic in peak power regulated systems (e.g. WiFi [8]); if the peak power is high compared to the average power, the overall

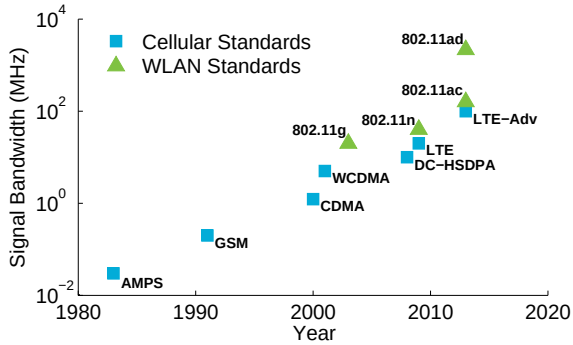

Figure 1.1: Evolution of cellular standards and wireless local area network (WLAN) standards in terms of signal bandwidth [9–14].

signal power has to be lowered to meet the regulation. The net effect of a high PAPR is decreased SNR in the communications channel. It also puts higher requirements on the circuit characterization in terms of dynamic range and linearity of the measurement instruments. The dynamics of a signal can be expressed in terms of its peak-to-average power ratio (PAPR), and Table 1.1 shows the PAPR of common cellular standards.

The two-dimensional increase in complexity of the communication signals, due to increased modulation and wider signal bandwidths, has serious implications on how microwave circuits operate as well as how they are designed and characterized. Linear and time invariant assumptions often fail because various nonlinear sources in the circuits are excited by the injected signals. Traditional characterization methods usually consist of S-parameter measurements for linear two-port transfer characteristics and two-tone measurements for characterization of circuit nonlinearity. Although they still are needed, these methods are nowadays often complemented with more advanced measurements, performed with e.g. a Nonlinear Vector Network Analyzer (NVNA). The NVNA gives useful insight in device behavior and has become a vital part in the microwave circuit design cycle, most prominently used for transistor modeling and high efficiency amplifier design [16]. However, the NVNA architecture is often intrinsically narrowband, and therefore unable to support the wider bandwidths that modern communication signals demand [17,18]. Hence, there is a need for wideband measurement systems for nonlinear circuit and component characterization at mm-wave carrier frequencies.

This thesis deals with the implementation of a vector-corrected two-port characterization setup with wideband, nonlinear measurement capabilities. An introduction to nonlinear measurements and contemporary two-port nonlin-

Table 1.1: Peak-to-average power ratios (PAPRs) for common cellular standards in uplink [15].

Cellular standard	GSM	EDGE	WCDMA	HSPA	LTE
PAPR	0 dB	3.2 dB	3.5-5.5 dB	4.9-7.2 dB	10 dB

ear measurement architectures is given in Chapter 2. The need of nonlinear characterization is motivated and advantages and disadvantages with each measurement architecture are compared and discussed. Chapter 3 gives a detailed description of the proposed vector-corrected two-port characterization setup. Based on results from Paper [A], the proposed setup is demonstrated by its use as an active load-pull setup with multi-band capabilities. Chapter 3 also describes improvements made to the proposed setup in Paper [B], by correcting magnitude and phase errors caused by the measurement receivers. Characterization of dispersive effects in GaN HEMTs is discussed in Chapter 4, and results from Paper [C] are presented. Finally, the thesis is concluded in Chapter 5 and future work is discussed.

Chapter 2

An Overview of Nonlinear RF Characterization

As motivated in the previous chapter, the importance of nonlinear RF characterization is continuously increasing due to the use of more complex signals. This chapter gives an introduction to nonlinear measurements and an overview of different nonlinear measurement system architectures used for two-port characterization of microwave devices. The focus throughout the thesis is put on the signal acquisition in measurement setups, rather than signal generation. Furthermore, since nonlinear characterization is a broad topic, this thesis addresses vector-corrected two-port nonlinear measurement setups. The development of such measurement setups has mainly focused on three different types: sampler-based architectures, mixer-based architectures and direct RF sampling architectures.

2.1 Introduction to Nonlinear Microwave Measurements

Measuring accurately and precisely knowing the output of a system for a given input signal is crucial for any hardware-driven industry. Components such as transistors need to be characterized, first of all to be verified against rigorous specifications and tolerances, but also to extract models used in simulations performed with computer-aided design (CAD) tools. The latter is fundamental in an efficient circuit design cycle.

Measurements at high frequencies are problematic due to a number of reasons: various parasitic inductances and capacitances limit frequency operating range; radiating emissions cause significant losses; imperfections in cables and other transmission structures cause losses and reflections; physical lengths have to be considered [19]. High frequency measurements on nonlinear circuits only inflate the problem since most instruments are designed with the linear framework in mind. This section explains and motivates the need of nonlinear measurements, starting from linear measurements.

2.1.1 Linear Networks

Since their establishment in the 1940s, S-parameters have become synonymous with microwave engineering. Used as a tool for describing linear transfer characteristics of a circuit, it has become well-established within the microwave community and used in nearly all microwave circuit characterization [20]. Instead of calculating ratios of currents and voltages, i.e. Z- and Y-parameters, S-parameters are based on ratios of forward and backward traveling voltage waves, normally denoted as a- and b-waves, respectively. This gives a number of advantages compared to voltage and current descriptions: 1.) Easier to define reference planes 2.) Easier to work with power relations 3.) Easier to measure accurately at high frequencies [21].

The S-parameters of a two-port network, which is the most common network type, are defined as

$$\begin{aligned} S_{11} &= \left.\frac{b_1}{a_1}\right|_{a_2=0} \quad S_{12} = \left.\frac{b_1}{a_2}\right|_{a_1=0} \\ S_{21} &= \left.\frac{b_2}{a_1}\right|_{a_2=0} \quad S_{22} = \left.\frac{b_2}{a_2}\right|_{a_1=0}, \end{aligned} \tag{2.1}$$

where a_1 and b_1 are the propagating waves at the reference plane of port 1, and a_2 and b_2 are the propagating waves at the reference plane of port 2. Another way of looking at (2.1) is to view a_1 and a_2 as stimuli signals, and b_1 and b_2 as responses of the network. The requirement of $a_1 = 0$ and $a_2 = 0$ is satisfied by terminating the non-excited port with a load with the same impedance as the system impedance, Z_0, usually 50 Ω.

S-parameters are built upon the superposition principle and therefore assume perfectly linear networks. A linear network response only contains scaled versions of the stimuli, i.e. magnitude and phase change. As such, measurements can be carried out one frequency at a time and subsequently combined to get the complete frequency response of the network for any input signal type. This is essentially how a vector network analyzer (VNA) operates, and is illustrated in Fig. 2.1, where the injected signals are frequency-swept sine waves. The two-port measurement architecture of a VNA is shown in Fig. 2.2. Couplers sense the propagating waves and stimuli is connected to the source ports, x_1 and x_2. The device under test (DUT) is connected between port 1 and port 2, also known as the DUT reference planes. The VNA uses tuned receivers, which incorporate mixers and local oscillators (LOs) locked to the frequency of the injected signals for coherent downconversion of the wave quantities. The output signal from the mixer is bandpass filtered to improve noise performance and an analog-to-digital converter (ADC) then performs the data acquisition [22]. The two-port measurement architecture makes it possible to define accurate reference planes and to perform calibration to remove systematic errors due to cables and couplers. The VNA, however, requires that no other signals, beside the excitation frequency, exist in the network being characterized. This type of characterization is thus only valid for linear networks.

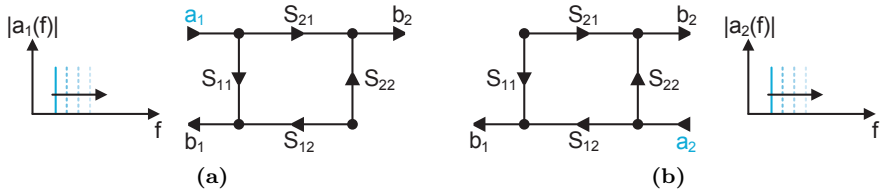

Figure 2.1: Signal flow graph showing the measurement procedure of two-port S-parameters, using a combination of two consecutive measurements. (a) Stimuli on port 1 (a_1), responses b_1 and b_2 are monitored. (b) Stimuli on port 2 (a_2), responses b_1 and b_2 are monitored.

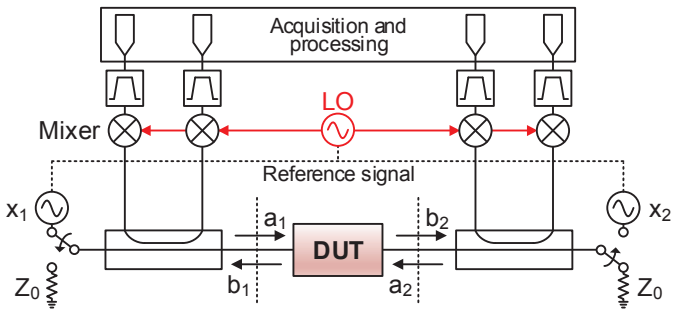

Figure 2.2: Vector network analyzer block diagram. The coupled RF signal is fed to mixers, which are pumped by a high power, high frequency LO. The signal sources, x_1 and x_2, and the LO are synchronized with a reference signal for coherent downconversion.

2.1.2 Nonlinear Networks, Basic Characterization

No network is perfectly linear and therefore an assumption is made for the VNA measurement that, if the stimuli is small enough, the network can be linearized at a given operating point. This is also known as small-signal operation. Nonlinear distortion is, however, always present and small-signal operation is in many cases a crude assumption. Since nonlinear phenomena are too general to give an overview of here, the nonlinearities discussed in this thesis only cover *periodic in, same periodic out* (PISPO) behavior [23].

The simplest periodic signal is a single sinusoid. The network response of a nonlinear circuit to a single-frequency sinusoid will contain frequency components harmonically related to the excitation signal, as shown in Fig. 2.3. The network has been simplified to a single-input (x) single-output (y) system, which is the case for a matched network ($S_{11} = 0$ and $S_{22} = 0$). The substitution $x = a_1$ and $y = b_2$ can be made if wanted. A simple model of the network response can be derived using a Taylor expansion, giving

$$y(t) = p_0 + p_1 x(t) + p_2 x(t)^2 + p_3 x(t)^3 + \ldots, \tag{2.2}$$

where p_0, p_1, p_2, p_3 are coefficients determining the amount of DC, fundamental, second, third harmonic content generated by the network. The Taylor

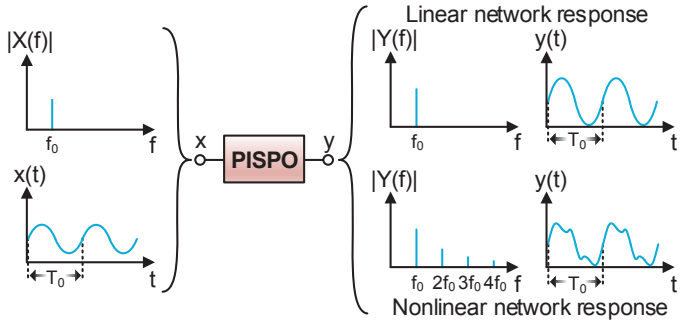

Figure 2.3: An example of a linear and nonlinear PISPO network response, with its time-domain representation denoted by $y(t)$ and frequency-domain representation denoted by $Y(f)$, to a single-frequency stimuli, $x(t)$ and $X(f)$.

series extends to infinity, but since the coefficients for higher order terms tend to be small, a limited number of coefficients can in most cases be considered.

Using a VNA to characterize a nonlinear network will lead to unreliable predictions about the actual network behavior. The purpose of a VNA measurement is essentially to determine the p_1-term of (2.2), and while nonlinear distortion in terms of compression can be measured to a certain degree by sweeping the stimuli power, the higher order terms are neglected.

The harmonic generation of a nonlinear network is typically characterized by using a spectrum analyzer, illustrated in Fig. 2.4. The stimuli is often a continuous wave (CW) signal generator, but can be interchanged with a vector signal generator (VSG) for advanced stimuli. The receiver of a spectrum analyzer performs a swept bandpass measurement similar to a VNA, but since the stimuli frequency is fixed with respect to the LO frequency, the harmonics will be visible in the measured frequency spectrum. This measurement procedure, however, lacks the possibility to extract detailed information of the measured network. Because the traveling wave quantities are not measured, the reference planes are not as accurately defined as for the VNA. This limits for example the opportunity to de-embed phase shifts due to cables. On the other hand, modern implementations of spectrum analyzers, e.g. vector signal analyzers (VSAs), offer the possibility to view the measured signals in time-domain, a feature which is not available for VNAs. This is, however, mainly limited to modulated signals as the analyzing bandwidth normally is a fraction of the carrier frequency. As such, the time-domain waveform for a high-frequency fundamental tone with harmonics is not recoverable with a VSA.

2.1.3 Nonlinear Networks, Full Characterization

As discussed in the previous section, measurement instruments such as the VNA and VSA are unfeasible for accurate characterization of nonlinear networks. This mainly due to two aspects: lack of fully calibrated waveform measurements, not only ratio-measurements (S-parameters); lack of frequency-domain to time-domain transformation. These aspects are important to resolve if the time voltage and current waveforms at the ports of the network

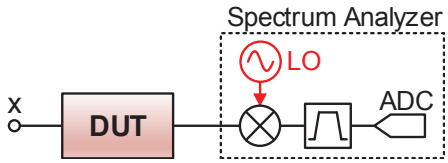

Figure 2.4: Circuit characterization using a spectrum analyzer. Stimuli is connected to the source port, x, and the spectrum analyzer measures the output generated by the DUT.

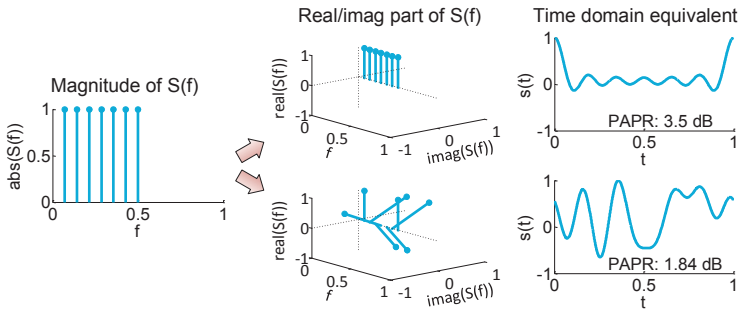

Figure 2.5: Two signals having the same magnitude spectrum but different cross-frequency phases, leading to different time domain equivalents.

are of interest. For example, in characterization of high efficiency amplifiers, such as switched-mode amplifiers, where the shape of the current and voltage waveforms determine the efficiency and output power performance [16]. Moreover, as described in Chapter 1, mobile communication signal complexity is increasing in terms of bandwidth and PAPR, also stressing the need of detailed time domain characterization. The first aspect is resolved with additional calibration of the measurement setup, and is described in detail in Chapter 3.

The time-domain representation is not possible to recover in a VNA, or a regular spectrum analyzer, due to the lack of cross-frequency phase information. An illustration of two signals with the same magnitude spectrum, but different cross-frequency phases is shown in Fig. 2.5. The time-domain equivalents can vastly differ depending on the cross-frequency phases, which in turn can have large impact on the corresponding output signals in a nonlinear network. The loss of cross-frequency phase information in a mixer-based down-converting receiver architecture can be explained by the following equation

$$y_{LO}(t) \times y_{RF}(t) = A_{LO}\cos(\omega_{LO}(t)t + \phi_{LO}(t)) \times \sum_{k=0}^{N} A_k \cos(w_k t + \phi_k), \quad (2.3)$$

where $y_{LO}(t)$ is the frequency-swept LO and $y_{RF}(t)$ the signal of interest, consisting of a number of discrete frequencies. The phase of the LO, $\phi_{LO}(t)$, is added to the phase of the downconverted signal, and since the LO-phase is

unknown and time-varying it will be impossible to distinguish from the phase of the signal of interest, ϕ_k.

Three measurement architectures that circumvent this problem are presented in the following section: sampler-based architectures, mixer-based architectures and direct RF sampling architectures. The main difference between these architectures is how acquisition of the RF signal is carried out. These systems, here referred to as two-port nonlinear measurement setups, can be seen as an extension of the conventional VNA, as they provide fully calibrated waveform measurements with time-domain capabilities.

2.2 Two-port Nonlinear Measurement Setups

Two-port nonlinear measurement setups, sometimes referred to as nonlinear vector network analyzers (NVNAs), can be separated into three categories: sampler-based, mixer-based and direct RF sampling setups. This section goes into detail of each setup type, describes the architectural differences and discusses the advantages and disadvantages with each approach.

2.2.1 Sampler-based Architectures

Sampler-based receivers became appealing for microwave frequencies with the introduction of the Hewlett-Packard microwave transition analyzer (MTA) in 1991, providing vectorial measurements with preserved cross-frequency phases up to 40 GHz [24]. A sampler-based two-port measurement setup is shown in Fig. 2.6. The RF-to-IF conversion is based on a sequential triggering of a sampling gate, which is placed after the sensing couplers. The trigger pulse is generated from a sampling frequency synthesizer, labeled f_s in Fig. 2.6, and is pulse-shaped to create steep pulse flanks. The sampling frequency can be several orders of magnitude lower than the RF frequency, hence why this technique is also known as sub-sampling. By choosing the sampling frequency in a sophisticated way and assuming periodicity of the measured signal, the high frequency content of the signal can be down-converted to a low frequency equivalent. From a time-domain perspective it can be seen as a successive sampling of the waveform, where the sampling instance moves forward relative to the measured signal for each period. The output of the sampler is low-pass filtered to improve noise performance and to suppress sampling frequency feedthrough. Finally, high resolution ADCs perform the data acquisition. The sampling clock and measurement receivers are synchronized with a reference clock, usually 10 MHz, for increased signal stability. The overall performance of sampler-based architectures is greatly dependent on well-defined pulses which trigger the sampling gates.

The pulse trigger can be described as a pulse train with a certain pulse width, τ, and a period time, $1/f_s$. The pulse train can be expressed in the frequency domain to determine the spectral content, and the amplitudes of the corresponding Fourier coefficients, C_k, vary with frequency according to

$$C_k = f_s \tau \frac{\sin(\pi k f_s \tau)}{\pi k f_s \tau}, \tag{2.4}$$

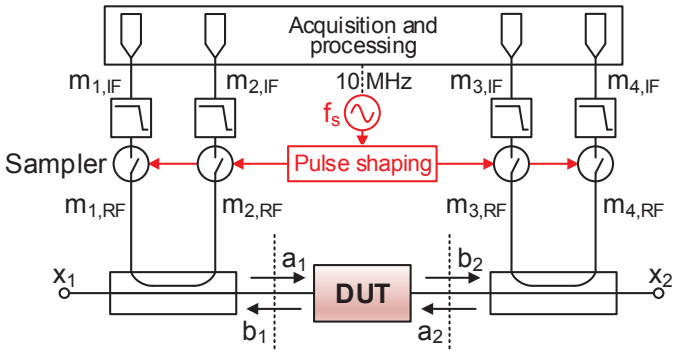

Figure 2.6: Sampler-based two-port nonlinear measurement setup. The RF signal, denoted by $m_{x,RF}$, is coupled and fed to the samplers, which are pulsed by a sampling clock, f_s. The sampling clock and receivers are synchronized with a 10 MHz clock for increased signal stability.

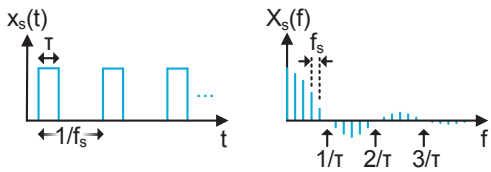

Figure 2.7: A generic pulse train with a pulse width of τ and period time of $1/f_s$. (Left) Time domain representation. (Right) Frequency domain representation.

where k is the Fourier coefficient index. A generic pulse train and its frequency-domain equivalent is shown in Fig. 2.7. The period time of the pulse train will determine the frequency spacing of the spectral components. As seen from Fig. 2.7, the first null of the fourier coefficients occurs at $1/\tau$. Consequently, if the pulse width becomes infinitely narrow, the null will move towards infinite frequency and the spectral components will have a uniform amplitude distribution. The pulse train can then be approximated as an impulse train, which is a train of Dirac pulses, to simplify the mathematical expressions.

The sampling gate can be seen as a mixing operation between the RF signal, $x_{RF}(t)$, and the Dirac pulses, $x_S(t)$, as

$$y_{IF}(t) = x_{RF}(t) \times x_S(t) = \sum_{k=0}^{N} A_k \cos(k\omega_{RF}t) \times \sum_{n=-\infty}^{\infty} \delta(t - nt_s) = \\ = \sum_{k=0}^{N} A_k \sum_{n=-\infty}^{\infty} \cos(k\omega_{RF}t)\delta(t - nt_s), \qquad (2.5)$$

where A_k are the amplitude coefficients for the RF signal, ω_{RF} is the fundamental RF angular frequency, k is the harmonic index, t_s is the period time of the Dirac pulses and n denotes the nth Dirac pulse. The RF signal consists

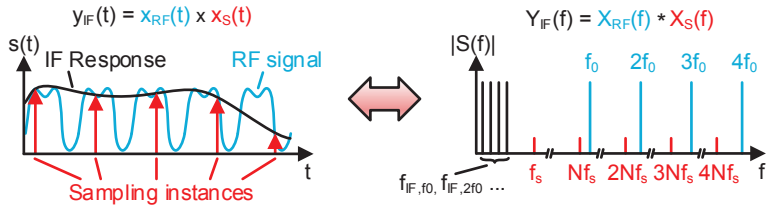

Figure 2.8: Illustration of the mixing operation in a sampling gate. (Left) Multiplication in time domain. (Right) Convolution in frequency domain.

of a fundamental tone and a number of harmonics. The mixing operation is visualized in Fig. 2.8. The multiplication in time domain will correspond to a convolution in the frequency domain. If the sampling frequency is chosen correctly, the spectrum of the pulse train and the RF signal will be situated on different frequency grids, causing the down-converted IF signal to appear at the following frequencies

$$f_{IF,k} = k(f_{RF} - Nf_s), \tag{2.6}$$

where k is the harmonic index of the RF signal and N denotes the Nth harmonic of the sampling frequency. Equation (2.6) can also be expressed as a modulo operation according to

$$f_{IF,k} = k \times \mathrm{mod}(f_{RF}, f_s). \tag{2.7}$$

Note that the above expression is valid for unmodulated RF signals. It is shown in [18] that a modulated multi-sine RF signal with a frequency content of $f_{RF,(k,m)} = kf_0 + mf_m$ will be downconverted to the following IF frequencies

$$\begin{cases} f_{IF,(k,m)} = k \times \mathrm{mod}(f_{RF}, f_s) + mf_m & \text{if } m \geq 0 \\ f_{IF,(k,m)} = -k \times \mathrm{mod}(f_{RF}, f_s) - mf_m & \text{if } m < 0 \end{cases}, \tag{2.8}$$

where m is the modulation frequency index ranging from $-M$ to M, giving a total modulation bandwidth of $2M$.

Due to the mathematical properties of the sub-sampling operation in sampler-based systems, it has spectral compression features which can be used to measure multi-harmonic or wideband modulated signals that have bandwidths many times higher than the ADC bandwidth. Mixer-based systems lack this feature, as will be described in the following section.

2.2.2 Mixer-based Architectures

Mixers are extensively used within the microwave community for various frequency conversion tasks. The objective of a mixer in a two-port measurement setup serves a similar purpose as the sampler; to convert high-frequency content of the measured signal to a low-frequency equivalent, which ADCs can sample with high fidelity. A mixer-based measurement setup is shown in Fig.

2.9. Couplers sense the propagating waves and the coupled signal is fed to a mixer, which is pumped by a high power RF LO source. The output of the mixer is bandpass filtered and digitized by the ADCs. In contrast to a sampler-based system, which compresses the measured RF signals into narrowband IF signals through sub-sampling, the architecture of a mixer-based system is slightly more complex. The down-conversion of a fundamental tone with harmonics requires sequential acquisitions of each harmonic, due to the lack of spectral compression and limitations in ADC bandwidth. As such, cross-frequency phase information is lost, as described in Section 2.1. This is addressed by using a fifth mixer and reference receiver, which performs down-conversion on a known, multi-harmonic signal [25].

A mixer can be modeled as a nonlinear network using a Taylor expansion as described by (2.2). The input to the mixer, $x(t)$, consists of a large signal LO, $x_{LO}(t)$, and a small signal RF, $x_{RF}(t)$, expressed as follows

$$x(t) = x_{LO}(t) + x_{RF}(t) = A_{LO}\cos(\omega_{LO}t + \phi_{LO}) + A_0\cos(\omega_0 t + \phi_0). \quad (2.9)$$

Assuming the same order of nonlinearity as in (2.2), the output signal of the mixer will be

$$\begin{aligned} y(t) = p_0 &+ p_1\left(A_{LO}\cos(\omega_{LO}t + \phi_{LO}) + A_0\cos(\omega_0 t + \phi_0)\right) \\ &+ p_2\left(A_{LO}\cos(\omega_{LO}t + \phi_{LO}) + A_0\cos(\omega_0 t + \phi_0)\right)^2 \\ &+ p_3\left(A_{LO}\cos(\omega_{LO}t + \phi_{LO}) + A_0\cos(\omega_0 t + \phi_0)\right)^3. \end{aligned} \quad (2.10)$$

The expression can expanded and rewritten with trigonometric identities as

$$\begin{aligned} y(t) = p_0 &\\ &+ p_1\left[A_{LO}\cos(\omega_{LO}t) + A_0\cos(\omega_0 t)\right] \\ &+ p_2\Big[A_{LO}A_0(\cos((\omega_{LO}-\omega_0)t) + \cos((\omega_{LO}+\omega_0)t)) \\ &+ \frac{1}{2}A_{LO}^2(1+\cos(2\omega_{LO}t)) + \frac{1}{2}A_0^2(1+\cos(2\omega_0 t))\Big] \\ &+ p_3\Big[A_{LO}^3\left(\frac{3}{4}\cos(\omega_{LO}t) + \frac{1}{4}\cos(3\omega_{LO}t)\right) \\ &+ A_0^3\left(\frac{3}{4}\cos(\omega_0 t) + \frac{1}{4}\cos(3\omega_0 t)\right) \\ &+ 3A_{LO}^2A_0\left(\frac{1}{2}\cos(\omega_0 t) + \frac{1}{4}\cos((2\omega_{LO}-\omega_0)t) + \frac{1}{4}\cos((2\omega_{LO}+\omega_0)t)\right) \\ &+ 3A_{LO}A_0^2\left(\frac{1}{2}\cos(\omega_{LO}t) + \frac{1}{4}\cos((2\omega_0-\omega_{LO})t) + \frac{1}{4}\cos((2\omega_0+\omega_{LO})t)\right)\Big]. \end{aligned} \quad (2.11)$$

As seen, the number of mixing frequencies grow exponentially with the order of nonlinearity. With modulated signals the expression becomes even more complicated and proper filtering is needed to avoid aliasing and saturation of the ADC. The bandwidth of the bandpass filter in Fig. 2.9 is selected to filter

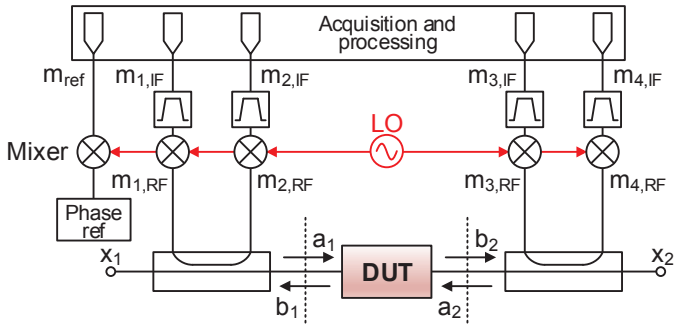

Figure 2.9: Mixer-based two-port nonlinear measurement setup. The coupled RF signal is fed to mixers, which are pumped by a high power, high frequency LO. The output from the mixers is bandpass-filtered and fed to the measurement receivers. A phase reference is connected to a fifth receiver for maintaining cross-frequency phase information.

out the frequencies of interest, in this case $\omega_0 - \omega_{LO}$. By generalizing (2.11), the output of the mixer will contain the following frequencies for a multi-sine input signal

$$f_{y,(r_{LO},r_k)} = r_{LO} f_{LO} + \sum_{k=1}^{N} r_k f_k \qquad (2.12)$$

$$\text{with} \quad |r_{LO}| + \sum_{k=1}^{N} |r_k| \leq \text{Order of nonlinearity},$$

where $f_{y,(r_{LO},r_k)}$ are the output frequencies of the mixer, f_{LO} is the local oscillator frequency, f_k is the kth multi-sine frequency and r_{LO} and r_k are integer numbers describing the mixing products.

2.2.3 Direct RF Sampling Architectures

Unlike sampler- and mixer-based setups, the direct RF sampling approach captures waveforms at RF frequencies without intermediate frequency conversion. These types of architectures are enabled by the rapid development of ADCs, and are currently supporting frequencies up to 100 GHz [26]. The waveform digitization is performed in the time-domain and thus the cross-frequency phase information is preserved, similar to sampler-based setups. A typical direct RF sampling setup is shown in Fig. 2.10. Most often oscilloscopes are used for signal acquisition, due to their compact form factor and that they are commonly configured with four signal ports, which make them suitable for calibrated two-port setups. Oscilloscopes come in two types: equivalent time sampling oscilloscopes and real time oscilloscopes (RTOs). In an equivalent time sampling oscilloscope, the sample rate is usually lower than the signal frequency, and the sampling instances are shifted relative to the signal, similar to what happens in a sampler-based setup. A drawback is that periodic signals are required, but the ADCs have higher bit resolution, commonly 14

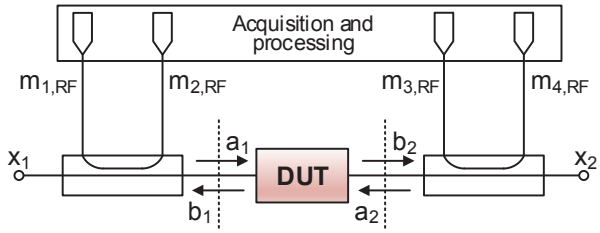

Figure 2.10: Direct RF sampling two-port nonlinear measurement setup. The coupled RF signal is directly fed to the measurement receivers, without any intermediate frequency conversion.

bits [27]. In an RTO, the sample rate needs to be at least two times as high as the highest frequency content in the measured signal, and the bit-resolution of the ADCs in high-speed RTOs is usually only around 8 bits. On the other hand, an advantage is that realistic non-periodic signals can be measured [28].

2.2.4 Discussion and Comparison

The nonlinear measurement architectures introduced in this chapter each have their advantages and disadvantages. While new methods improving certain shortcomings, such as bandwidth limitations, are continuously published, there are still some fundamental differences bound to the architecture being used.

In terms of setup simplicity, direct RF sampling and sampler-based systems are straight-forward as they do not require any phase synchronization between harmonics. This is a major difference compared to mixer-based setups, where a fifth measurement receiver and an external reference is needed to synchronize the phase of measured tones in order to reconstruct time domain waveforms.

Mixer- and sampler-based architectures are preferable for accurate signal acquisition, attributed to the high bit-resolution of the ADCs in the measurement receivers. This, however, leads to an inherent IF bandwidth limitation, as there is a trade-off between sample rate and bit-resolution in ADCs [29]. On the other hand, sampler-based systems compress the frequency spectrum during downconversion, and can therefore cover wide modulation bandwidths using proper sample clock settings. Furthermore, bandwidth extension techniques have been developed for sampler-based systems [30–32]. The direct RF architecture has an advantage in terms of instantaneous bandwidth, i.e. bandwidth covered in one ADC acquisition cycle, and is therefore a very flexible solution which can be utilized to measure both periodic and non-periodic signals. It lacks, however, performance in terms of dynamic range as the bit-resolution is lower than for mixer- or sampler-based systems. Various signal processing techniques, such as waveform averaging, can improve the dynamic range of direct RF sampling systems [33]. Direct RF systems based on RTOs might be unfeasible as signal frequencies approach >10 GHz, due to the Nyquist sampling rate criterion. Sampling at twice the signal frequency requires extreme amounts of memory and data processing capabilities, although sub-sampling techniques can relax these requirements.

In terms of noise performance, mixer-based systems have, in theory, the lowest noise floor due to the narrowband filtering in the IF stage. Actual noise performance will however depend on the RF frontend. Sampler-based systems have a higher noise floor due to noise folding in the subsampling operation. The noise performance in direct RF sampling systems rely heavily on the frontend, but is in general worse than mixer-based and sampler-based systems due to the large receiver bandwidth.

To put the measurement setup presented in this thesis into context, Table 2.1 has been compiled to give an overview of previous studies and commercially available systems. There is a slight over-representation of mixer- and sampler-based systems, with no commercial instruments being based on a direct RF sampling principle. This is reasonable, given the high RF bandwidth of those systems. As previously discussed, direct RF sampling using RTOs are unfeasible for signals with extremely high frequency content. There is, however, a clear trend in recent years of pushing the IF bandwidth of mixer- and sampler-based setups to >100 MHz. Examples of these are the Maury Microwave MT4463 [34] and the Anritsu MS464xB Series [35]. While the measurement setup presented in this thesis, which is based on a direct RF principle, may not be able to compete with mixer- and sampler-based systems in terms of noise floor and raw ADC performance, it still is appealing due to the simplicity and flexibility of the measurement receiver.

Table 2.1: A brief overview of nonlinear measurement setups developed over recent years.

Author/Product	Year	Architecture	State	RF BW (GHz)	IF BW (GHz)	ADC resolution
M. Sipilä et al. [36]	1988	Direct RF	Academic	14	14	-
U. Lott [37]	1989	Mixer	Academic	15	-	-
G. Kompa, F. Van Raay [38]	1990	Mixer + Direct RF	Academic	20	-	-
F. Van Raay, G. Kompa [39]	1992	Sampler	Academic	40	0.01	10 bits
J. Verspecht et al. [40]	1995	Sampler	Academic	18	0.004	23 bits
J. Benedikt et al. [41]	2000	Sampler	Academic	40	0.01	10 bits
M. Marchetti et al. [42]	2008	Mixer	Academic	6	0.045	14 bits
Maury Microwave LSNA [43]	2004	Sampler	Commercial	50	0.01	14 bits
VTD SWAP X-402 [17]	2008	Sampler	Commercial	30	0.05	-
Maury Microwave MT4463 [34]	2014	Mixer	Commercial	40	0.24	14 bits
Keysight Technologies [44]	2014	Mixer	Commercial	50	0.015	-
Rohde & Schwarz [45]	2015	Mixer	Commercial	67	0.005	-
Anritsu [35]	2015	Sampler	Commercial*	70	0.198	14 bits
This work	**2013**	**Direct RF**	**Academic**	**4**	**4**	**8 bits**

*Not advertised as a nonlinear measurement setup. However, its high speed digitizers can be used for wideband characterization.

Chapter 3

Wideband Two-port Nonlinear Measurement Setup

The development of advanced nonlinear measurement setups is an ongoing research topic. As discussed in the previous chapter, there exists no ideal architecture and optimization of various performance aspects are trade-offs of each other. Due to the complexity of communication signals and nonlinear phenomena, the end application will often set the requirements on the nonlinear characterization setup.

The wideband two-port nonlinear measurement setup presented in this thesis is based on a direct RF sampling architecture, giving a large instantaneous bandwidth and flexibility in the choice of stimuli. First, an overview of the measurement setup is given and the two-port calibration procedure is presented. Later, an oscilloscope correction method is presented, which improves the signal fidelity over a large dynamic range.

Finally, the wideband capabilities of the system are demonstrated by configuring the system as an active load-pull setup, with the possibility of tuning the load reflection coefficients at intermodulation frequencies.

3.1 System Description

The wideband two-port nonlinear measurement system is based on a direct RF sampling architecture, as shown in Fig. 3.1. The measurement receiver is a real time oscilloscope; Rohde & Schwarz RTO1044 with 4 channels, 4 GHz bandwidth and up to 10 GSa/s sampling rate. The memory depth of each channel is 100 MSa. The ADCs of the RTO have 8 bit resolution and an effective number of bits (ENOB) of $\geq$7 [46]. This gives an SNR of roughly 50 dB and a signal-to-noise-and-distortion ratio (SNDR) of roughly 44 dB [47]. The SNR can be improved by waveform averaging using periodic signals. The signal generation is handled by an arbitrary waveform generator (AWG) from Keysight Technologies, Model M8190A. It has a maximum sampling frequency of 8 GSa/s with 14 bit digital-to-analog (DAC) resolution, 5 GHz analog band-

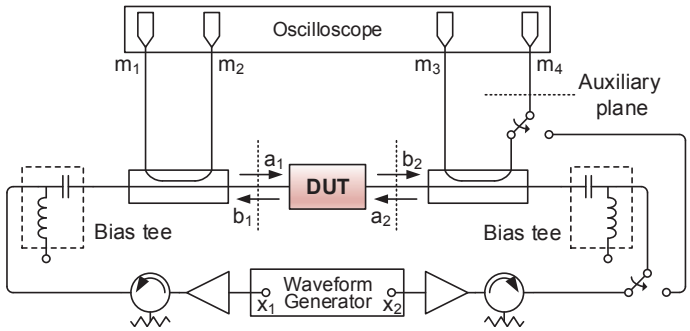

Figure 3.1: Overview of the wideband two-port nonlinear measurement setup, configured with external bias tees and amplifiers and isolators on the arbitrary waveform generator (AWG) outputs. The auxiliary path is used for absolute magnitude and phase calibration.

width and a memory depth of 2 GSa per channel. The large memory depth and high sampling frequency makes it possible to synthesize complex modulated signals, such as W-CDMA or LTE, directly at RF frequencies without an upconverting stage. The AWG also has built-in amplifiers to increase the signal power level [48]. External driver amplifiers are however used during measurements with high power requirements, such as load-pull.

In the current system configuration the frequency range is mainly limited by the couplers, which cover 300 MHz–3800 MHz. The driver amplifiers and isolators can be multiplexed to cover large parts of the excitation bandwidth. As such, the measurement setup as a whole can characterize devices over a wide bandwidth in a single measurement, without system re-configuration. There are no step-attenuators in the signal paths before the oscilloscope. Instead, the internal variable gain amplifiers (VGAs) of the RTO are used for signal leveling. The acquired waveforms are post-processed using an external computer, where calibration and correction algorithms are applied.

The frequency resolution, or frequency bin size, of the measured spectrum, Δf, is determined by the sampling frequency and number of samples of the oscilloscope as

$$\Delta f = \frac{f_s}{N_s}, \tag{3.1}$$

where f_s is the sampling frequency of the RTO and N_s is the number of acquired samples. The frequency bin size of the oscilloscope and AWG are preferably aligned within integer multiples of each other to reduce FFT leakage. The large memory depth of the RTO makes it possible to achieve a frequency resolution of 100 Hz at full sampling rate.

3.2 Two-port Calibration Procedure

To ensure reliable measurements with the system, a calibration is needed. Calibration algorithms for conventional VNAs have been extensively studied since the 1950s [49], and many of those techniques can be applied to nonlinear measurement setups as well, with some slight modifications.

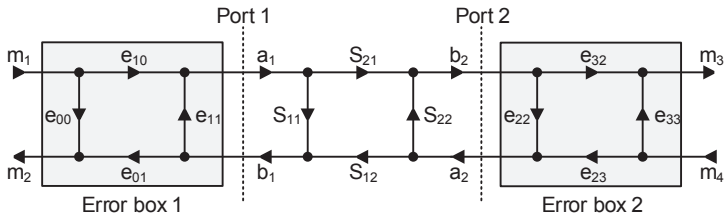

Figure 3.2: Signal flow graph showing the error models of the systematic errors in the measurement setup.

The system calibration is a two-stage procedure, where the first step is a relative calibration at the DUT ports and the second step is an absolute calibration with a power meter and phase reference. The relative calibration aims to remove all systematic errors due to cables and couplers, and makes it possible to measure ratioed quantities, e.g. $S_{11} = b_1/a_1$. A conventional VNA requires only a relative calibration. In nonlinear two-port measurement setups, however, an absolute calibration is required since the power and cross-frequency phase information of the wave quantities is wanted. The calibration techniques described in this section are not unique to this measurement setup, and techniques discussed here can readily be applied to other systems as well. It should also be noted that the calibration procedure originates from [50] and [51].

The algorithm for the relative calibration can be of any type: short-open-load-through (SOLT), short-open-load-reciprocal (SOLR), through-reflect-line (TRL), line-reflect-match (LRM) and so forth [25, 49]. The SOLR algorithm is presented here due to its mathematical clarity. The calibration of the system is made under the assumption that the measurement receivers operate in the linear region, both during the calibration procedure and during the DUT measurements. The user must make sure that enough attenuation is inserted before the receivers. Most RTOs have built-in VGAs in the signal paths for gain adjustment, which can be used to ensure that the signal is within the operating range of the ADCs. Furthermore, uncontrollable variations such as self-heating and change in ambient temperature are assumed to be negligible. The isolation between measurement channel pairs m_1 and m_2, and m_3 and m_4 is assumed to be good enough.

The systematic errors of the measurement system can be modelled as two error boxes, one for each DUT port as seen in Fig. 3.2. The calibration procedure is carried out one frequency at a time, and combined to obtain the complete frequency dependence of the error boxes. The system error model can mathematically be described as follows

$$\begin{bmatrix} \tilde{a}_1 \\ \tilde{b}_1 \\ \tilde{a}_2 \\ \tilde{b}_2 \end{bmatrix} = \begin{bmatrix} \frac{1}{e_{10}e_{01}} \begin{pmatrix} -\Delta_x & e_{11} \\ -e_{00} & 1 \end{pmatrix} & 0 \\ 0 & \frac{c_{thru}}{e_{32}e_{23}} \begin{pmatrix} -\Delta_y & e_{22} \\ -e_{33} & 1 \end{pmatrix} \end{bmatrix} \begin{bmatrix} m_1 \\ m_2 \\ m_4 \\ m_3 \end{bmatrix}, \tag{3.2}$$

where $\Delta_x = e_{00}e_{11} - e_{10}e_{01}$, $\Delta_y = e_{22}e_{33} - e_{32}e_{23}$ and c_{thru} is a normalizing factor so that waves at port 1 and port 2 can be compared. The tilde-sign

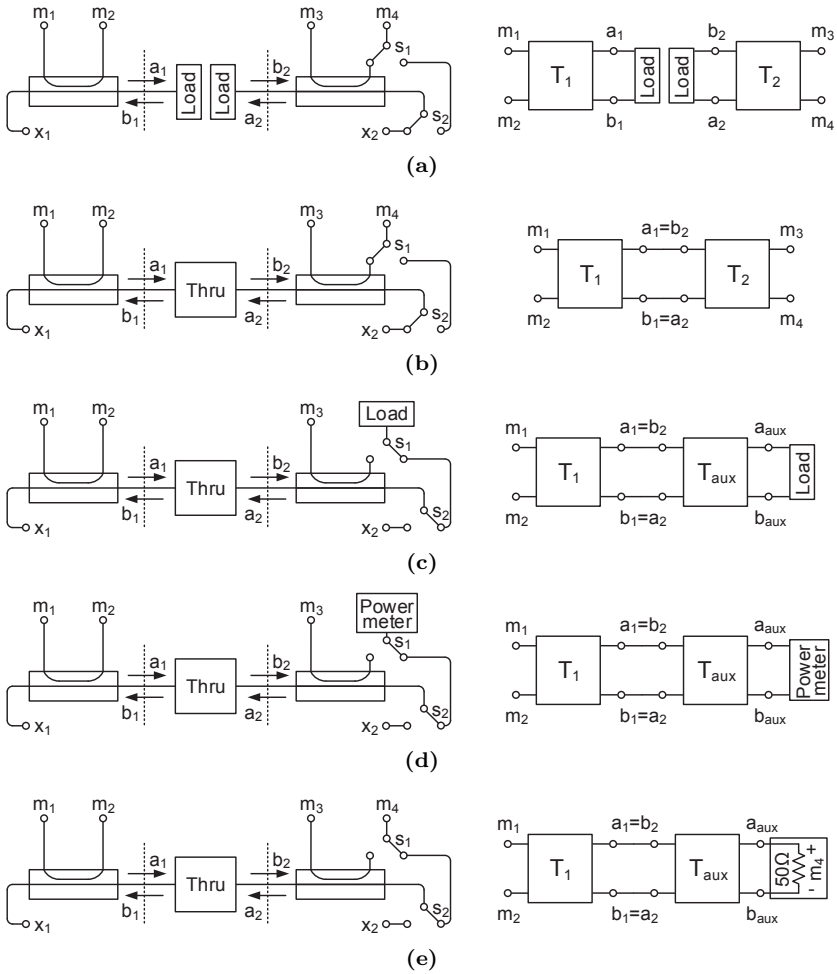

Figure 3.3: Calibration procedure of the measurement setup: (a) Relative calibration at DUT ports. (b) Relative calibration, unknown through. (c) Intermediate calibration at auxiliary plane. (d) Absolute magnitude calibration with power meter. (e) Absolute phase calibration with fourth receiver as reference.

above each wave quantity indicates that absolute calibration is not yet applied. All of the error terms except c_{thru} are extracted from two separate short-open-load (SOL) calibrations at each DUT port, and is shown in Fig. 3.3a. The c_{thru}-term is determined by an unknown-through measurement, and is shown in Fig. 3.3b.

The SOL calibration at each port can be set up in the following way to extract the error terms, exemplified here at port 1 as

$$\begin{bmatrix} \Gamma_{m,short} \\ \Gamma_{m,open} \\ \Gamma_{m,load} \end{bmatrix} = \begin{bmatrix} 1 & \Gamma_{L,short} \times \Gamma_{m,short} & -\Gamma_{L,short} \\ 1 & \Gamma_{L,open} \times \Gamma_{m,open} & -\Gamma_{L,open} \\ 1 & \Gamma_{L,load} \times \Gamma_{m,load} & -\Gamma_{L,load} \end{bmatrix} \begin{bmatrix} e_{00} \\ e_{11} \\ \Delta_x \end{bmatrix}, \tag{3.3}$$

where $\Gamma_{L,short}$, $\Gamma_{L,open}$, $\Gamma_{L,load}$ are the reflection coefficients of the short, open and load terminations, respectively, and $\Gamma_{m,short}$, $\Gamma_{m,open}$, $\Gamma_{m,load}$ the measured reflection coefficients of the corresponding terminations. The reflection coefficients of the terminations are ideally $\Gamma_{L,short} = -1$, $\Gamma_{L,open} = 1$ and $\Gamma_{L,load} = 0$. However, they are often described with equivalent circuit models or tabulated for increased calibration accuracy.

The c_{thru}-term can be determined from a measurement using a reciprocal transmission line, also known as an unknown-through calibration. By describing the signal flow graph in Fig. 3.2 with scattering transfer parameters (T-parameters) and using the same definitions as in (3.2), the following equation can be set up

$$\boldsymbol{T_m} = c_{thru}\boldsymbol{T_1}^{-1}\boldsymbol{T_{DUT}}\boldsymbol{T_2} \tag{3.4}$$

where $\boldsymbol{T_m}$ is the measured T-parameter matrix, $\boldsymbol{T_1}$ is the T-parameter matrix for error box 1, $\boldsymbol{T_2}$ is the T-parameter matrix for error box 2 and $\boldsymbol{T_{DUT}}$ is the T-parameter matrix for the through transmission line. Since $\boldsymbol{T_{DUT}}$ is reciprocal, the determinant of it is equal to unity. As such, taking the determinant of the left hand side and right hand side of (3.4) leads to

$$\det(\boldsymbol{T_m}) = \det(c_{thru}\boldsymbol{T_1}^{-1}\boldsymbol{T_{DUT}}\boldsymbol{T_2}) = c_{thru}^2 \det(\boldsymbol{T_1})^{-1} \det(\boldsymbol{T_2}), \tag{3.5}$$

and solving for c_{thru} finally results in

$$c_{thru} = \pm\sqrt{\frac{\det(\boldsymbol{T_m})\det(\boldsymbol{T_1})}{\det(\boldsymbol{T_2})}}. \tag{3.6}$$

The sign ambiguity requires only rough knowledge of the unknown through S_{21}-phase, and the selection procedure is described in detail in [50, 52].

The next stage in the calibration procedure is to perform the absolute calibration, which determines the α-term in the equation below

$$\begin{bmatrix} a_1 \\ b_1 \\ a_2 \\ b_2 \end{bmatrix} = \alpha \begin{bmatrix} \tilde{a}_1 \\ \tilde{b}_1 \\ \tilde{a}_2 \\ \tilde{b}_2 \end{bmatrix}, \tag{3.7}$$

where the tilde-denoted variables are the wave quantities with relative calibration applied from (3.2).

In the first step of the absolute calibration an auxiliary plane is defined where the power and phase calibration is to be made, shown in Fig. 3.1. The introduction of an auxiliary plane gives an advantage for this measurement system, namely that the fourth oscilloscope port can be used as a reference port for the phase calibration. Hence, no external phase reference is needed. This is based on the assumption that all measurement receivers of the oscilloscope are fully synchronized, which usually is the case for modern oscilloscopes [51]. Furthermore, for on-wafer measurements an auxiliary plane is necessary since power meters and phase references usually come with coaxial or waveguide interfaces [25].

An SOL calibration is made at the auxiliary plane with a through-line connected to the DUT ports and the switches (s_1 and s_2) toggled, solving the

error box $\boldsymbol{T_{aux}}$ shown in Fig. 3.3c. The following error matrix is used for the $\boldsymbol{T_{aux}}$ error box

$$\begin{bmatrix} a_{aux} \\ b_{aux} \end{bmatrix} = \alpha_r \left[\frac{1}{r_{10} r_{01}} \begin{pmatrix} -\Delta_{aux} & r_{11} \\ -r_{00} & 1 \end{pmatrix} \right] \begin{bmatrix} m_1 \\ m_2 \end{bmatrix} = \alpha_r \begin{bmatrix} \tilde{a}_{aux} \\ \tilde{b}_{aux} \end{bmatrix}, \tag{3.8}$$

where a_{aux} and b_{aux} are the traveling voltage waves at the auxiliary reference plane, α_r contains the absolute magnitude and phase information referenced to the auxiliary plane and $\tilde{a}_{aux}$ and $\tilde{b}_{aux}$ are the measured traveling voltage waves with relative auxiliary calibration applied. The magnitude of α_r is determined using a power meter, shown in Fig. 3.3d, as follows

$$P_{ref} = \frac{|\alpha_r \tilde{a}_{aux}|^2 - |\alpha_r \tilde{b}_{aux}|^2}{2Z_0} \Longrightarrow |\alpha_r| = \sqrt{\frac{2Z_0 P_{ref}}{|\tilde{a}_{aux}|^2 - |\tilde{b}_{aux}|^2}}, \tag{3.9}$$

where P_{ref} is the power measured by the power meter and Z_0 is the system impedance. The determination of the phase of α_r is based on the assumption that the oscilloscope is well calibrated, and therefore $m_4 = a_{aux} + b_{aux}$ as shown in Fig. 3.3e. Using (3.8), the phase is resolved as

$$\angle\alpha_r = \arg\left(\frac{m_4}{\frac{1}{r_{10} r_{01}} \big(m_2(1 + r_{11}) - m_1(r_{00} + \Delta_{aux}) \big)} \right). \tag{3.10}$$

The α_r-term can now be referenced back to the DUT ports to obtain α as

$$\alpha = \alpha_r \sqrt{\frac{\det(\boldsymbol{T_{aux}})}{\det(\boldsymbol{T_1})}}. \tag{3.11}$$

The system is now calibrated and ready to perform measurements. However, some additional correction algorithms are introduced, based on results from Paper [B].

3.3 Correction Algorithms

To increase the usable dynamic range of a nonlinear measurement system, pre-calibrated step attenuators are often placed in the signal path before the measurement receivers. Input power sweeps over a wide range can therefore be carried out without being limited by ADC quantization noise. In the proposed wideband nonlinear measurement setup, no step attenuators are used. Instead, the internal VGAs of the oscilloscope are used. The block diagram of the front-end of an RTO is shown in Fig. 3.4. A course adjustment is first made with an attenuator, followed by a VGA for fine adjustment. In the current implementation of the system, only the VGA is used.

However, in Paper [B] we noted a couple of issues related to using the internal gain control. Depending on the circuitry of the instrument, the input impedance of the measurement ports can vary versus the gain control setting for certain oscilloscopes, as shown in Fig. 3.5. The gain control setting is here expressed as voltage range setting (mV), also known as vertical scale, of the oscilloscope. This is problematic for vector-corrected two-port measurement

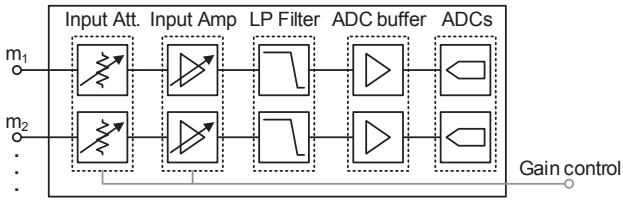

Figure 3.4: Typical block diagram of the front-end of a real-time oscilloscope. The input signal to the ADCs can be adjusted in two steps, course adjustment with an attenuator and fine adjustment with VGAs. The low-pass filter has a cut-off frequency slightly above the analog bandwidth of the oscilloscope to prevent aliasing.

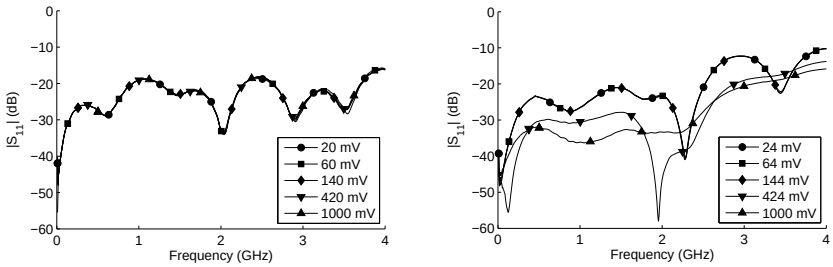

(a) **(b)**

Figure 3.5: Port match versus frequency for two different oscilloscopes with different voltage range settings. (a) Oscilloscope A. (b) Oscilloscope B.

systems, since the change in port match will invalidate the error coefficients obtained from the system calibration. The oscilloscope used in the current system implementation has a constant port match versus voltage range setting, as seen in Fig. 3.5a. Furthermore, in [B] we also show that the VGA introduces a complex gain to the measured signal, which is not compensated for by the self-calibration procedures that instrument suppliers integrate into the oscilloscopes. Depending on the frequency of the input signal and the gain control setting, magnitude and phase errors can be up to 0.6 dB and 15.7 °, respectively, for this particular oscilloscope. A method which corrects for the complex gain caused by the VGA is proposed in [B]. The implementation is based on lookup-tables extracted from measurements referenced to a power meter and one of the oscilloscope ports. The procedure for extracting the correction factors for the look-up table is simple, as it only requires two external instruments; a CW signal generator and a power meter.

The extraction of the correction factors is carried out as follows. First, the magnitude of the correction factors are determined by monitoring the discrepancy in measured power between a power meter and one of the oscilloscope ports. The measurement setup is shown in Fig. 3.6a. The output of the signal generator is connected to a two-way power splitter, which in turn is connected to the power meter and one of the oscilloscope ports. The measurement procedure is described in a flow diagram shown in Fig. 3.7a. A suitable

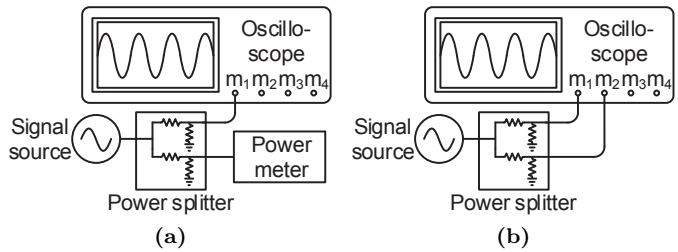

Figure 3.6: Measurement setup for extracting the correction factors. (a) Magnitude discrepancy measurement. (b) Phase discrepancy measurement.

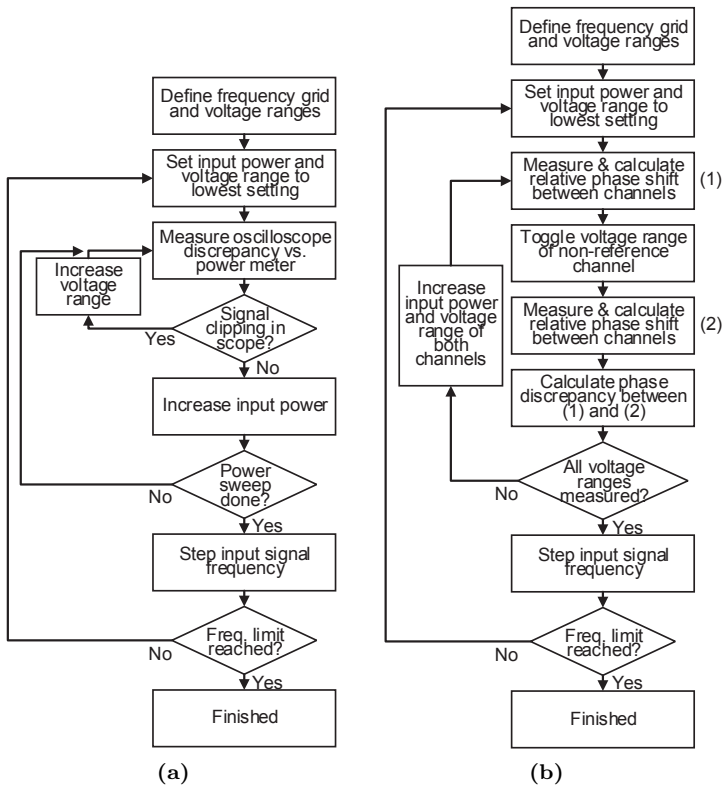

Figure 3.7: Flow diagram of the measurement procedure for extracting the correction factors. (a) Magnitude discrepancy measurement. (b) Phase discrepancy measurement.

frequency grid and voltage range grid is chosen and the input power is set to the minimum detectable power of the oscilloscope. The discrepancy versus the power meter is monitored whilst the input power is swept. The voltage range of the oscilloscope is increased if the input signal is clipping. The procedure is repeated for each frequency and oscilloscope port. The phase of the correction factors is determined using two of the oscilloscope channels, utilizing one as a reference port and one as a measurement port, connected to the power

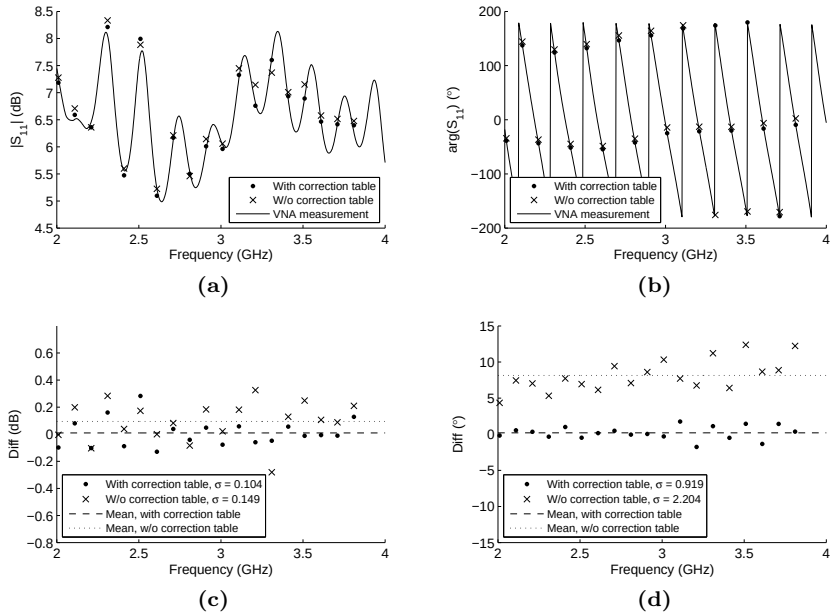

Figure 3.8: Measured S-parameters of a reflection amplifier. The measurements show a VNA trace and two traces with the wideband nonlinear measurement system, with and without correction enabled. (a) Magnitude of S_{11}. (b) Phase of S_{11}. (c) Magnitude of S_{11}, discrepancy versus VNA. (d) Phase of S_{11}, discrepancy versus VNA.

splitter as shown in Fig. 3.6b. The flow diagram in Fig. 3.7b describes the measurement procedure. The same frequency grid and voltage range grid is used as for the previous measurement. The voltage range of the reference port is set to a constant value, meanwhile the voltage range of the other port is toggled between two values. The relative phase change between these two cases is monitored. The input power is increased and the voltage range of both channels is stepped to the next value. The procedure is repeated for each frequency and oscilloscope port.

After obtaining the magnitude and phase of the correction factors, raw measurement data from the oscilloscope is corrected as

$$\begin{bmatrix} \hat{m}_1 \\ \hat{m}_2 \\ \hat{m}_3 \\ \hat{m}_4 \end{bmatrix} = \begin{bmatrix} k_{1,x} & 0 & 0 & 0 \\ 0 & k_{2,y} & 0 & 0 \\ 0 & 0 & k_{3,z} & 0 \\ 0 & 0 & 0 & k_{4,w} \end{bmatrix} \begin{bmatrix} m_{1,x} \\ m_{2,y} \\ m_{3,z} \\ m_{4,w} \end{bmatrix}, \tag{3.12}$$

where $k_{1,x}$, $k_{2,y}$, $k_{3,z}$, $k_{4,w}$ are the complex correction factors for each channel at voltage ranges x, y, z, w. The corrected oscilloscope measurements are denoted as $\hat{m}_1$, $\hat{m}_2$, $\hat{m}_3$, $\hat{m}_4$.

The method was verified by measuring a one-port device, with and without correction enabled. The device was a reflection amplifier with a reflection coefficient greater than unity. The results are shown in Fig. 3.8. A large im-

provement is seen in the measured S_{11}-phase with correction enabled, resulting in a mean error of roughly zero degrees. The mean and standard deviation of the measured magnitude is improved as well.

3.4 System Demonstration: Multi-band Load-pull

As motivated in the introduction, the importance of wideband characterization is increasing due to the bandwidth expansion communication signals. Modern cellular standards use wider bandwidths in order to enable higher data rates. Since the frequency spectrum at current operating frequencies is limited and extremely crowded, fragmented spectrum allocation techniques such as carrier aggregation are being implemented in the most recent cellular standards [6]. Hence, relevant device characterization must be carried out to investigate the effect of concurrent operation with several frequency bands, i.e. concurrent multi-band operation. In this section results from Paper [A] are presented, where the wideband two-port nonlinear measurement setup is used for multi-band load-pull characterization of a gallium nitride (GaN) high electron mobility transistor (HEMT).

Load-pull is a common technique where the load impedance of a device is systematically varied, for example in order to optimize a transistor for maximum output power or maximum efficiency, as these are load-dependent quantities. Instead of using a passive load, such as an impedance tuner, active load-pull generates the load with active signal injection [53]. The working principle can be seen from the following equation

$$\Gamma_L(f_0) = \frac{a_2(f_0)}{b_2(f_0)} = \frac{Ae^{(2\pi f_0 + \phi)}}{b_2(f_0)}, \tag{3.13}$$

where $\Gamma_L(f_0)$ is the load impedance seen by the device at frequency f_0 and $a_2(f_0)$, $b_2(f_0)$ the propagating waves at port 2. By monitoring the outwards propagating wave generated by the device, $b_2(f_0)$, and controlling the amplitude, A, and phase, ϕ, of the injected signal on port 2, $a_2(f_0)$, the load reflection coefficient can be tuned as desired.

The active signal injection can be carried out using a closed-loop configuration or an open-loop configuration. For closed-loop active signal injection, a portion of the DUT-generated wave (b_2) is coupled from the signal path, adjusted in amplitude and phase and then re-injected to the device. In an open-loop configuration, the injected signal is instead synthesized by an external signal generator. The closed-loop configuration is in general faster at providing the wanted reflection coefficient to the DUT, but can be prone to oscillations if not proper filtering is implemented. The bandwidth of the closed-loop configuration is also a limiting factor. The open-loop configuration, on the other hand, can be very wideband and does not suffer from oscillations. However, since the actively injected signal is not based on the DUT-generated wave, a couple of iterations is needed before the actual load reflection coefficient converges to the wanted load reflection coefficient [42].

Commonly, a single fundamental tone is injected into the device, and the load impedance is controlled at the fundamental frequency and harmonics.

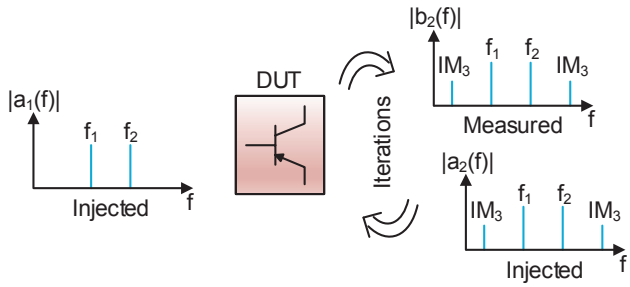

Figure 3.9: Illustration of the active load-pull multi-band concept. A high power two-tone is injected into the DUT, generating amplified versions of the fundamental tones as well as IM3 products. The load impedances are controlled by active signal injection at the fundamental and IM3 frequencies.

It is a well-established method to increase the output power and efficiency of a device. As discussed in [54], controlling the load impedances at intermodulation frequencies can aid in understanding phenomena such as spectral regrowth asymmetry. In Paper [A] we carried out concurrent multi-band load-pull, where two tones ($f_1 = 2.14$ GHz and $f_2 = 2.65$ GHz) were simultaneously injected into the device, as illustrated in Fig. 3.9. The load impedances at both fundamental and third order intermodulation (IM3) frequencies were tuned. Although simplified using only two tones, this procedure is quite intricate as the load impedances were simultaneously controlled at the fundamental frequencies and IM3 products. Due to bandwidth limitations in the pre-driver amplifiers, the load impedances at second order intermodulation frequencies could not be controlled, and were instead kept close to 50 Ω. The load impedances at harmonic products were also kept close to 50 Ω.

The measurements were carried out on a commercial 6 W GaN HEMT, with a quiescent bias corresponding to Class AB operation. First, to demonstrate the importance of considering concurrent multi-band load-pull, a comparison between single-tone load-pull at each fundamental frequency and simultaneous two-tone load-pull was made. The fundamental load impedances were optimized for maximum total efficiency, expressed as follows for the concurrent load-pull case

$$\eta_{total} = \frac{P_{out,2.14} + P_{out,2.65}}{P_{DC} + P_{in,2.14} + P_{in,2.65}}, \tag{3.14}$$

where $P_{out,2.14}$ is the RF output power at the first fundamental frequency (2.14 GHz), $P_{out,2.65}$ is the RF output power at the second fundamental frequency (2.65 GHz), P_{DC} is the DC power consumption, $P_{in,2.14}$ is the RF input power at the first fundamental frequency and $P_{in,2.65}$ is the RF input power at the second fundamental frequency. The results of the single-tone load-pull and concurrent multi-band load-pull are shown in Fig. 3.10. There is a slight, but noticeable shift in optimal load impedance between the two modes of operation. This is an important conclusion to take into account when designing amplifiers for concurrent multi-band operation.

Next, load-pull at the IM3 frequencies (1.63 GHz and 3.16 GHz) was carried out with the load impedance at the fundamental tones set to the optimized

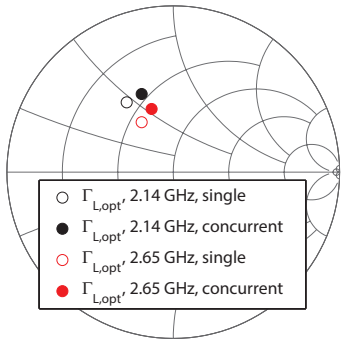

Figure 3.10: Optimal load reflection coefficient for highest total efficiency for single-tone operation and dual-band concurrent operation.

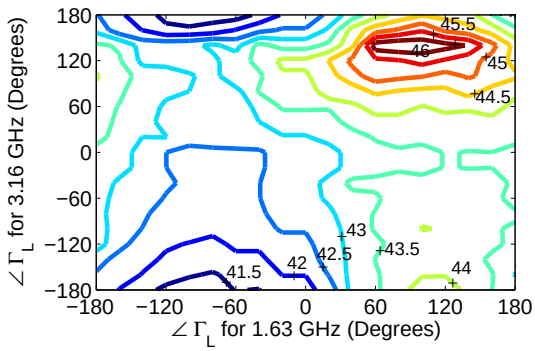

Figure 3.11: IM3 load-pull result showing total efficiency (%) versus the angle of the load reflection coefficients at the intermodulation products.

value for maximum total efficiency. To avoid power dissipation at the intermodulation frequencies, the load impedances at these frequencies were tuned purely reactive. As such, the IM3 load impedances were swept along the periphery of the Smith chart, implying a unity magnitude and a phase sweep from $-180°$ to $180°$ of the load reflection coefficients. The total efficiency was monitored for each measurement. The efficiency contours are shown in Fig. 3.11, where the x-axis and y-axis corresponds to the phase of the load reflection coefficient at 1.63 GHz and 3.16 GHz, respectively. The total efficiency varies from 41.5% to 46% with the maximum at $\Gamma_{L,1.63} = 1\angle 80°$ and $\Gamma_{L,3.16} = 1\angle 140°$. The efficiency enhancement due to proper IM3 termination is not significant, and a circuit implementation using this type of termination might exhibit even lower efficiency enhancement due to extra losses associated with the IM3 termination network. It is, however, a good proof-of-concept for demonstrating the wideband capabilities of the measurement system. It will enable future research activities within wideband device characterization and aid in the design of high performance microwave circuits.

Chapter 4

Dispersive Effects in GaN HEMTs

GaN-based HEMTs are promising candidates for being the preferred technology for high frequency and power performance applications. This is due to the exceptional properties of the GaN semiconductor material: high breakdown field, high electron saturation velocity and good thermal conductivity. The material has matured greatly during the last decade, resulting in devices with RF output power of up to 40 W/mm and f_t/f_{max} of up to 450/600 GHz [55, 56]. It is, however, well known that several trapping mechanisms are present in GaN HEMTs, causing severe discrepancy between DC current-voltage (I-V) characteristics and RF I-V characteristics. Such phenomena, also known as dispersion, is a major limitation in GaN HEMTs, as it restricts the current and voltage swing in the device, effectively limiting the RF output power [57]. Understanding the trapping mechanisms and coping with it is therefore of outermost importance for the widespread adoption of GaN HEMTs in wireless systems.

Characterization of dispersive effects is a comprehensive subject since the phenomena results in complex device behavior, with a lot of variable parameters that can influence the results. For example, thermal effects in the devices are often hard to exclude during large signal operation or when using hot bias points. Characterization setups and measurement methods targeting specific dispersive effects have been developed in order to isolate different effects from each other and to facilitate the tedious task of describing and understanding dispersive phenomena. In Paper [C] we investigated how such phenomena manifest on various DC and RF performance aspects, using different measurement setups.

4.1 Understanding Dispersive Effects in GaN HEMTs

Trapping mechanisms in GaN HEMTs have been extensively studied and characterized, and are usually correlated to charge trapping centers at the surface or buffer of the device. The trapping centers are highlighted in Fig. 4.1, which

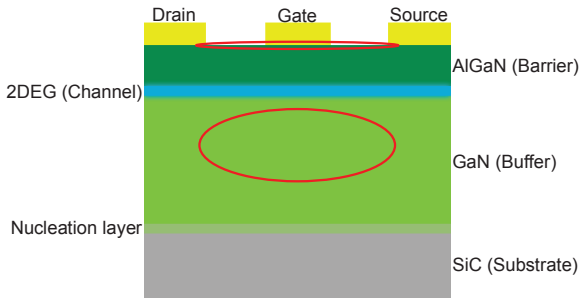

Figure 4.1: Cross-sectional view of a AlGaN/GaN HEMT grown on a SiC substrate. Common trapping centers are marked with red circles.

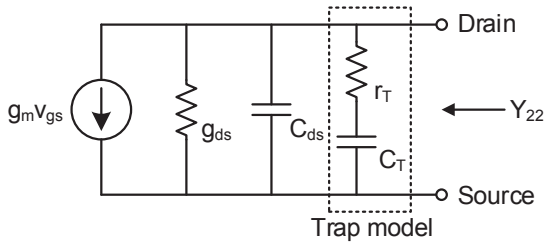

Figure 4.2: Small signal circuit model for output admittance dispersion, showing the drain side of a FET.

shows a cross-sectional view of a AlGaN/GaN HEMT grown on silicon carbide (SiC). Traps are usually linked with material defects, such as impurities, dislocations and intrinsic defects [57]. Studies have also shown that defects are present near the AlGaN barrier layer and the two-dimensional electron gas (2DEG) interface, but no degradation on microwave performance has been linked to these defects [57].

Trapping in HEMTs and field effect transistors (FETs) are known to cause dispersion in the output admittance of the device. To extract qualitative information about these mechanisms, dispersion due to a single-charge trapping center can be modelled as a RC-net between the drain and source, as shown in Fig. 4.2 [58]. The output admittance can be determined as follows

$$Y_{22}(\omega) = \left[g_m + g_{ds} + \frac{\omega^2 C_T/\omega_c}{1+(\omega/\omega_c)^2} \right] + j \left[\omega C_{ds} + \frac{\omega C_T}{1+(\omega/\omega_c)^2} \right], \qquad (4.1)$$

where g_m is the transconductance, g_{ds} is the output conductance, ω is the angular frequency, C_T the modeled dispersion capacitance, ω_c is the characteristic angular frequency and C_{ds} is the output capacitance. If the sum of g_m and g_{ds} are large at low frequencies, the phase of the output admittance will have a maximum at the characteristic frequency. As discussed in [59], the peak of the phase is correlated with the trap emission rate and hence it will follow a temperature dependence. By measuring the phase of the output admittance at different temperatures, and plotting the obtained peaks versus temperature, the activation energy of the traps can be extracted. This plot, also known as an Arrhenius diagram, is commonly used for analyzing temperature dependent

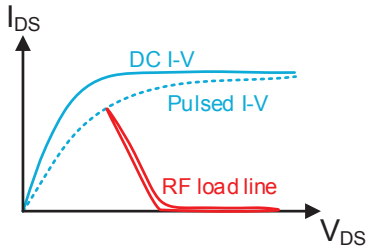

Figure 4.3: Drain current and drain voltage characteristics showing the effect of current collapse and knee walkout for three types of measurements: DC, pulsed I-V and RF.

reactions [60]. The activation energy can disclose valuable information about the defect linked to the trap [58].

Trapping also cause current collapse (CC) and knee walkout, which leads to major limitations in RF output power as the voltage and current trajectories are restricted. The effect is visualized in Fig. 4.3. The maximum RF output power can show severe discrepancy versus the maximum current and voltage swing for the DC case. Instead of measuring this discrepancy with a RF measurement setup, a pulsed I-V setup can be used. The purpose of this measurement is to mimic dynamic signals by performing a fast sweep of the I-V characteristics. As such, measurements can be carried out faster and the pulsed I-V setup is often simpler than an RF characterization setup. Typically, both the gate and drain voltages are pulsed at the same time, and different quiescent biases can be used to trigger certain trapping mechanisms.

4.2 Characterizing Dispersive Effects

In Paper [C] we investigated the influence of carbon doping in the GaN HEMT buffer on dispersive effects. Introducing an intentional dopant such as carbon yields high resistive buffers, improving breakdown characteristics and minimizing buffer leakage. As such, RF performance is enhanced. Three epitaxial structures were manufactured in Paper [C] with different carbon doping: 1) One with uniform high doping, denoted as High-C, 2) one with uniform low doping, denoted as Low-C and 3) one with stepped doping, denoted as Stepped-C. The in-house processed HEMTs had a gate length of 0.2 μm and a total gate width of 50 μm.

First, the output admittance dispersion was investigated. The Y-parameters were obtained from S-parameters, which were measured using a VNA with low-frequency measurement capabilities (3 Hz–3 GHz). The HEMTs were placed on a thermal chuck, of which the temperature was swept from 20 °C to 160 °C. The measurements are shown in Fig. 4.4. The High-C and Low-C HEMTs both show dispersion peaks consistently shifting versus temperature, indicating trap presence. The Stepped-C HEMT did not show such behavior. The activation energies of the traps were found to be $E_2 = 0.59$ eV and $D_1 = 0.15$ eV. Both traps are consistent with other studies, where it is speculated that they are related to defects in the GaN material. The E_2-trap is suggested to be

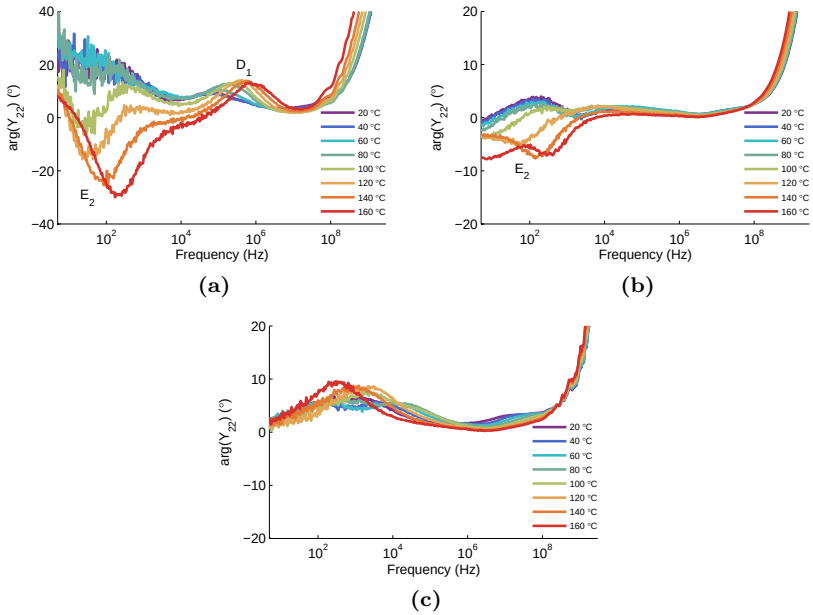

Figure 4.4: Phase of output admittance versus frequency for different chuck temperatures, swept from 20 °C to 160 °C. (a) High-C. (b) Low-C. (c) Stepped-C.

located in the buffer of the device, whereas the D_1-trap is suggested to be located at the surface of the device.

Device performance under dynamical conditions was assessed with pulsed I-V and load-pull measurements. Pulsed I-V measurements were carried out to investigate CC and knee walkout effects under off-state quiescent bias conditions. The dynamic I-V behavior for five different quiescent states is shown in Fig. 4.5. The quiescent states are marked within parenthesis as (V_{GS},V_{DS}). As expected from previous characterization, the High-C HEMT suffers from severe CC, dropping to about 75% of the reference measurement, denoted as (0,0). The large increase in on-resistance also confirms that the D_1-trap is located at the surface, as this is a typical behavior caused by surface traps [57]. The other devices show very slight CC and almost no increase in on-resistance. Large signal RF performance was determined using active load-pull, with the devices biased in class AB operation. An input power sweep at a fundamental frequency of 3 GHz is shown in Fig. 4.6, where the load reflection coefficients are optimized for maximum output power. The maximum output power for each device is in good agreement with estimates from pulsed I-V measurements. The maximum output power is approximately 0.9 W/mm, 2.4 W/mm and 2.3 W/mm for High-C, Low-C and Stepped-C, respectively.

GaN-based devices are important components for building future wireless systems. The widespread adoption of GaN is mainly limited by the severe dispersive effects, which cause complex device behavior. Optimized buffers using carbon doping can mitigate some of the effects, lowering current collapse without sacrificing device performance. Further buffer optimization is nonetheless

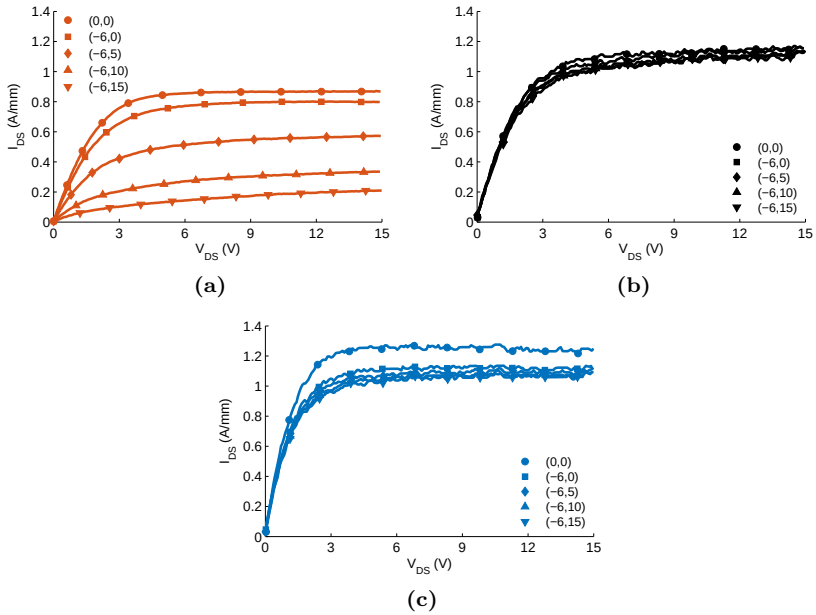

Figure 4.5: Pulsed I-V measurements showing the dynamic I_{DS}-V_{DS} behavior for various quiescent states. Quiescent states indicated within parenthesis as (V_{GS},V_{DS}). (a) High-C. (b) Low-C. (c) Stepped-C.

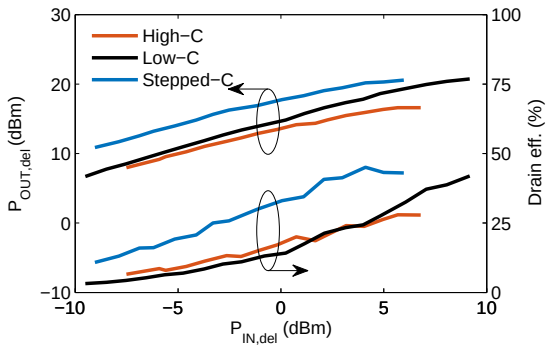

Figure 4.6: Delivered output power and drain efficiency versus delivered input power with load impedances optimized for maximum output power.

required to fully explore the possibilities of GaN devices using carbon-doped buffers.

As seen from the characterization results, dispersive effects can be very dynamic and sensitive to the stimuli. While measurement setups such as pulsed I-V and low-frequency VNAs are important for isolating certain effects and analyzing them in detail, there is also a need for a more unified approach using wideband stimuli, as this often the end application case for microwave devices in modern wireless systems. For example, a basic measurement such

as the output admittance dispersion measurement can show extreme dynamics when considering thermal effects, with responses ranging from 10 Hz to 1 MHz. Other studies have shown that self-heating effects on its own can be very dynamic, requiring characterization bandwidths of up to 100 MHz [61–63]. Other effects such as drain lag have become more important to consider in recent years. Drain lag is a CC-related effect, where high drain voltage pulsing can cause buffer trapping, leading to a transient response in the recovery of the drain current [57]. Due to the large amplitude fluctuations in modern communication signals, drain lag can have serious impact on system operability. With wideband characterization using realistic communication signals, such effects can be genuinely studied.

Chapter 5

Conclusions

This thesis has aimed to provide new wideband characterization tools for microwave circuits, and the main focus of the thesis is on the implementation of a vector-corrected two-port nonlinear measurement setup. It is based on a real-time oscilloscope and targets characterization using wideband signals, rather than multi-harmonic measurements that most research has focused on so far. Although multi-harmonic characterization is important for certain aspects, the trend in increased signal bandwidth in cellular standards is clear. Hence, there is a growing demand for measurement setups with wideband receivers. The setup was successfully demonstrated by its use as an active load-pull setup, where the reflection coefficients at intermodulation frequencies were tuned to improve total efficiency of a GaN HEMT. Improvements were made to the setup by introducing a correction technique which compensates nonidealities in the RF front-end of the oscilloscope. As such, signal fidelity is improved over a large dynamic range.

For the widespread adoption of the GaN semiconductor material, it is of importance to fully understand the dispersive effects that are present in GaN-based devices. Investigations on how dispersive effects manifest on various DC and RF performance aspects were carried out, using different measurement setups. The characterization was performed on in-house processed GaN HEMTs with carbon-doped buffers. The large dynamics of the dispersion cause complex device behavior, and while specific measurement instruments are needed to extract qualitative information about different trapping mechanisms, there is a need for wideband device characterization using realistic communication signals to evaluate practical system performance. With some further improvements to the proposed measurement setup, such as a low-frequency extension, detailed characterization of the slow and fast dynamics of dispersive effects will be enabled.

Based on the results of this thesis, future research activities within wideband device characterization will be possible using the proposed two-port nonlinear measurement setup. Wideband characterization is a necessity for the design of high performance wireless systems.

5.1 Future Work

There is a large interest in using the proposed two-port nonlinear measurement setup for various application-oriented characterization, and therefore further development of the system is needed. Increasing the measurement bandwidth is of importance for upcoming research activities, and there is a strong incentive for extending both the upper and lower frequency limits of the system. The lower cut-off frequency is mainly limited by the directional couplers, as the coupling factor rapidly degrades when approaching low frequencies. Measuring spectral regrowth at baseband frequencies has proven to give useful insight into dispersive effects in transistors. With this low-frequency extension, more detailed characterization of GaN devices can be carried out using realistic stimuli signals. Going up in frequency on the other hand, is motivated by the microwave industry due to the next generation communication standards which are planned to operate at mm-wave frequencies. Equipping the measurement system with a downconversion stage before the measurement receivers is therefore necessary.

Acknowledgment

I would like to express my gratitude to the people that made this work possible.

First of all, I would like to thank examiner Prof. Herbert Zirath and Prof. Jan Grahn for giving me the opportunity to conduct my research at the Microwave Electronics Laboratory.

I am also very grateful to supervisor Assoc. Prof. Christian Fager and co-supervisors Asst. Prof. Mattias Thorsell and Dr. Jörgen Stenarson for their excellent supervision and guidance through my academic career. Your different backgrounds have given me a great broadness in my academic viewpoint, and you have been a great source of inspiration and knowledge. I would also like to thank Assoc. Prof. Niklas Rorsman for interesting discussions and valuable feedback. Jan Andersson and Henric Fjellstedt are acknowledged for the superb and open-minded IT-support.

Thanks to my colleagues at MEL for creating a good and fun atmosphere, both professionally and outside the lab. I have enjoyed every day at work thanks to you.

Dedicated to Elin, my family and friends for the encouragement and support during my academic years.

This research has been carried out in the GigaHertz centre in a joint research project financed by Swedish Governmental Agency of Innovation Systems (VINNOVA), Chalmers University of Technology, Classic WBG Semiconductors AB, Comheat Microwave AB, Ericsson AB, Infineon Technologies Austria AG, Mitsubishi Electric Corporation, Saab AB, SP Technical Research Institute of Sweden, and United Monolithic Semiconductors.

Bibliography

[1] Cisco Systems Inc., "Cisco Visual Networking Index: Global Mobile Data Traffic Forecast Update 2014-2019 White Paper," Tech. Rep., 2015.

[2] GSMA Intelligence, "The Mobile Economy 2014," Tech. Rep., 2014.

[3] ——, "The Mobile Economy 2015," Tech. Rep., 2015.

[4] United Nations, "Concise Report on the World Population Situation in 2014," Tech. Rep., 2014.

[5] C. Shannon, "Communication in the Presence of Noise," *Proceedings of the IRE*, vol. 37, no. 1, pp. 10–21, Jan. 1949.

[6] Ericsson, "LTE Release 13, White Paper," Tech. Rep., 2015.

[7] T. S. Rappaport, R. Mayzus, Y. Azar, K. Wang, G. N. Wong, J. K. Schulz, M. Samimi, and F. Gutierrez, "Millimeter Wave Mobile Communications for 5G Cellular: It Will Work!" *IEEE Access*, vol. 1, pp. 335–349, 2013.

[8] Federal Communications Commision, *§15.247 Operation within the bands 902-928 MHz, 2400-2483.5 MHz, and 5725-5850 MHz.*, 2013.

[9] C. T. Bhunia, *Information Technology Network And Internet.* New Age International, 2006.

[10] E. Dahlman, P. Beming, J. Knutsson, F. Ovesjo, M. Persson, and C. Roobol, "WCDMA-the radio interface for future mobile multimedia communications," *IEEE Transactions on Vehicular Technology*, vol. 47, no. 4, pp. 1105–1118, 1998.

[11] A. M. Rao, A. Weber, S. Gollamudi, and R. Soni, "LTE and HSPA+: Revolutionary and evolutionary solutions for global mobile broadband," *Bell Labs Technical Journal*, vol. 13, no. 4, pp. 7–34, Feb. 2009.

[12] S. Parkvall, E. Dahlman, A. Furuskar, Y. Jading, M. Olsson, S. Wanstedt, and K. Zangi, "LTE-Advanced - Evolving LTE towards IMT-Advanced," in *2008 IEEE 68th Vehicular Technology Conference.* IEEE, Sep. 2008, pp. 1–5.

[13] Tektronix Inc., "Wi-Fi : Overview of the 802 . 11 Physical Layer and Transmitter Measurements," Tech. Rep., 2013.

[14] Agilent Technologies, *Wireless LAN at 60 GHz - IEEE 802 . 11ad Explained, Application Note*, 2013.

[15] E. McCune, "Modern cellular wireless signals," in *75th ARFTG Microwave Measurement Conference*. IEEE, May 2010, pp. 1–7.

[16] P. Tasker, "Practical waveform engineering," *IEEE Microwave Magazine*, vol. 10, no. 7, pp. 65–76, Dec. 2009.

[17] P. Roblin, Y. Ko, C. Yang, I. Suh, and S. Doo, "NVNA Techniques for Pulsed RF Measurements," *IEEE Microwave Magazine*, vol. 12, no. 2, pp. 65–76, Apr. 2011.

[18] J. Verspecht, "The return of the sampling frequency convertor," in *Conference, 2003. Fall 2003. 62nd ARFTG Microwave Measurements.* IEEE, 2003, pp. 155–164.

[19] V. Teppati, A. Ferrero, and M. Sayed, *Modern RF and Microwave Measurement Techniques*. Cambridge University Press, 2013.

[20] V. Belevitch, "Summary of the History of Circuit Theory," *Proceedings of the IRE*, vol. 50, no. 5, pp. 848–855, May 1962.

[21] Hewlett Packard, *Application Note 95-1, S-Parameter Techniques for Faster, More Accurate Network Design*, 1967.

[22] Rohde & Schwarz USA Inc., *Fundamentals of Vector Network Analysis*, 1st ed. Rohde & Schwarz USA Inc., 2011.

[23] J. Schoukens, R. Pintelon, T. Dobrowiecki, and Y. Rolain, "Identification of linear systems with nonlinear distortions," *Automatica*, vol. 41, no. 3, pp. 491–504, Mar. 2005.

[24] Hewlett Packard, *The Microwave Transition Analyzer: A Versatile Measurement Set for Bench and Test*, 1991.

[25] P. Roblin, *Nonlinear RF Circuits and Nonlinear Vector Network Analyzers*. Cambridge: Cambridge University Press, 2011.

[26] Teledyne LeCroy, *LabMaster 10 Zi-A Datasheet*, 2015.

[27] Keysight Technologies, *Infiniium DCA-X 86100D Wide-Bandwidth Oscilloscope Mainframe and Modules Data Sheet*, 2015.

[28] Agilent Technologies, *Application Note 5989-8794, What is the difference between an equivalent time sampling oscilloscope and a real-time oscilloscope?*, 2013.

[29] W. Kester, "Which ADC Architecture Is Right for Your Application ?" Tech. Rep., 2005.

[30] K. Remley, M. Schreurs, D. Williams, and J. Wood, "Extended NVNA bandwidth for long-term memory measurements," in *2004 IEEE MTT-S International Microwave Symposium Digest (IEEE Cat. No.04CH37535)*, vol. 3. IEEE, 2004, pp. 1739–1742.

[31] K. Remley, D. Williams, D. Schreurs, and M. Myslinski, "Measurement Bandwidth Extension Using Multisine Signals: Propagation of Error," *IEEE Transactions on Microwave Theory and Techniques*, vol. 58, no. 2, pp. 458–467, Feb. 2010.

[32] W. Van Moer and Y. Rolain, "An Improved Broadband Conversion Scheme for the Large-Signal Network Analyzer," *IEEE Transactions on Instrumentation and Measurement*, vol. 58, no. 2, pp. 483–487, Feb. 2009.

[33] C. Fager and K. Andersson, "Improvement of Oscilloscope Based RF Measurements by Statistical Averaging Techniques," in *2006 IEEE MTT-S International Microwave Symposium Digest.* IEEE, 2006, pp. 1460–1463.

[34] Maury Microwave, *MT2000 Data Sheet*, 2014.

[35] Anritsu, *MS464xB Series Microwave Vector Network Analyzers Datasheet*, 2015.

[36] M. Sipila, K. Lehtinen, and V. Porra, "High-frequency periodic time-domain waveform measurement system," *IEEE Transactions on Microwave Theory and Techniques*, vol. 36, no. 10, pp. 1397–1405, 1988.

[37] U. Lott, "Measurement of magnitude and phase of harmonics generated in nonlinear microwave two-ports," *IEEE Transactions on Microwave Theory and Techniques*, vol. 37, no. 10, pp. 1506–1511, 1989.

[38] G. Kompa and F. van Raay, "Error-corrected large-signal waveform measurement system combining network analyzer and sampling oscilloscope capabilities," *IEEE Transactions on Microwave Theory and Techniques*, vol. 38, no. 4, pp. 358–365, Apr. 1990.

[39] F. van Raay and G. Kompa, "A new on-wafer large-signal waveform measurement system with 40 GHz harmonic bandwidth," in *1992 IEEE Microwave Symposium Digest MTT-S.* IEEE, 1992, pp. 1435–1438.

[40] J. Verspecht, P. Debie, A. Barel, and L. Martens, "Accurate on wafer measurement of phase and amplitude of the spectral components of incident and scattered voltage waves at the signal ports of a nonlinear microwave device," in *Proceedings of 1995 IEEE MTT-S International Microwave Symposium.* IEEE, 1995, pp. 1029–1032.

[41] J. Benedikt, R. Gaddi, P. Tasker, and M. Goss, "High-power time-domain measurement system with active harmonic load-pull for high-efficiency base-station amplifier design," *IEEE Transactions on Microwave Theory and Techniques*, vol. 48, no. 12, pp. 2617–2624, 2000.

[42] M. Marchetti, M. Pelk, K. Buisman, W. Neo, M. Spirito, and L. de Vreede, "Active Harmonic Load-Pull With Realistic Wideband Communications Signals," *IEEE Transactions on Microwave Theory and Techniques*, vol. 56, no. 12, pp. 2979–2988, Dec. 2008.

[43] Maury Microwave, *MT4463 Data Sheet*, 2004.

[44] Keysight Technologies, *N5245A Data Sheet*, 2014.

[45] Rohde & Schwarz, *ZVA Vector Network Analyzer Data Sheet*, 2015.

[46] ——, *RTO Digital Oscilloscope Datasheet*, 2015.

[47] W. Kester, "Understand SINAD, ENOB, SNR, THD, THD + N, and SFDR so You Don't Get Lost in the Noise Floor," Tech. Rep., 2008.

[48] Keysight Technologies, *M8190A Arbitrary Waveform Generator Data Sheet*, 2014.

[49] A. Rumiantsev and N. Ridler, "VNA calibration," *IEEE Microwave Magazine*, vol. 9, no. 3, pp. 86–99, Jun. 2008.

[50] A. Ferrero and U. Pisani, "Two-port network analyzer calibration using an unknown 'thru'," *IEEE Microwave and Guided Wave Letters*, vol. 2, no. 12, pp. 505–507, Dec. 1992.

[51] K. Andersson and C. Fager, "Oscilloscope based two-port measurement system using error-corrected modulated signals," in *2012 Workshop on Integrated Nonlinear Microwave and Millimetre-wave Circuits*. IEEE, Sep. 2012, pp. 1–3.

[52] J. Stenarson and K. Yhland, "Automatic root selection for the unknown thru algorithm," in *2006 67th ARFTG Conference*. IEEE, Jun. 2006, pp. 150–155.

[53] Y. Takayama, "A New Load-Pull Characterization Method for Microwave Power Transistors," in *MTT-S International Microwave Symposium Digest*, vol. 76. MTT005, 1976, pp. 218–220.

[54] N. Borges de Carvalho and J. Pedro, "A comprehensive explanation of distortion sideband asymmetries," *IEEE Transactions on Microwave Theory and Techniques*, vol. 50, no. 9, pp. 2090–2101, Sep. 2002.

[55] K. Shinohara, D. C. Regan, Y. Tang, A. L. Corrion, D. F. Brown, J. C. Wong, J. F. Robinson, H. H. Fung, A. Schmitz, T. C. Oh, S. J. Kim, P. S. Chen, R. G. Nagele, A. D. Margomenos, and M. Micovic, "Scaling of GaN HEMTs and Schottky Diodes for Submillimeter-Wave MMIC Applications," *IEEE Transactions on Electron Devices*, vol. 60, no. 10, pp. 2982–2996, Oct. 2013.

[56] Y.-f. Wu, M. Moore, A. Saxler, T. Wisleder, and P. Parikh, "40-W/mm Double Field-plated GaN HEMTs," in *2006 64th Device Research Conference*. IEEE, Jun. 2006, pp. 151–152.

[57] S. Binari, P. Klein, and T. Kazior, "Trapping effects in GaN and SiC microwave FETs," *Proceedings of the IEEE*, vol. 90, no. 6, pp. 1048–1058, Jun. 2002.

[58] G. Umana-Membreno, J. Dell, B. Nener, L. Faraone, G. Parish, Y.-F. Wu, and U. Mishra, "Low-temperature shallow-trap related output-admittance frequency dispersion in AlGaN/GaN MODFETs," in *1998 Conference on Optoelectronic and Microelectronic Materials and Devices. Proceedings (Cat. No.98EX140)*. IEEE, 1998, pp. 252–255.

[59] K. Doverspike, S. Binari, and W. Kruppa, "Low-frequency dispersion characteristics of GaN HFETs," *Electronics Letters*, vol. 31, no. 22, pp. 1951–1952, Oct. 1995.

[60] L. G. Arnaut, S. J. Formosinho, and H. Burrows, *Chemical Kinetics: From Molecular Structure to Chemical Reactivity*, 2006.

[61] Y.-R. Wu and J. Singh, "Transient study of self-heating effects in AlGaN/GaN HFETs: Consequence of carrier velocities, temperature, and device performance," *Journal of Applied Physics*, vol. 101, no. 11, p. 113712, Jun. 2007.

[62] L. Ardaravicius, A. Matulionis, J. Liberis, O. Kiprijanovic, M. Ramonas, L. F. Eastman, J. R. Shealy, and A. Vertiatchikh, "Electron drift velocity in AlGaN/GaN channel at high electric fields," *Applied Physics Letters*, vol. 83, no. 19, p. 4038, Nov. 2003.

[63] M. Thorsell, K. Andersson, H. Hjelmgren, and N. Rorsman, "Electrothermal Access Resistance Model for GaN-Based HEMTs," *IEEE Transactions on Electron Devices*, vol. 58, no. 2, pp. 466–472, Feb. 2011.